SCHOOL OF ADVANCED STUDIES OF THE ROMANIAN ACADEMY

DOCTORAL SCHOOL OF CHEMICAL SCIENCES

PETRU PONI INSTITUTE OF MACROMOLECULAR CHEMISTRY

CHEMISTRY Field

POLYMERIC NANOCOMPOSITES WITH (PHOTO)CATALYTIC PROPERTIES

SUMMARY OF DOCTORAL THESIS

SCIENTIFIC COORDINATOR:
DR. ING. VALERIA HARABAGIU

Ph.D. STUDENT
GRECU IONELA

2026

ROMANIAN ACADEMY

„Petru Poni" Institute of Macromolecular Chemistry Iași

Mrs./Ms. .....

We hereby inform you that on the day of 27.02.2026 at 12^{00}, in the Conference Room of the "Petru Poni" Institute of Macromolecular Chemistry in Iași, the public defense of the doctoral thesis "***Polymeric Nanocomposites with (Photo)catalytic Properties***", authored by **Ionela Grecu**, will take place, for the purpose of obtaining the scientific title of doctor.

PRESIDENT: CS I Dr. Maria CAZACU

Institutul de Chimie Macromoleculară „Petru Poni" Iași

DOCTORAL SUPERVISOR: CS I Dr. Valeria HARABAGIU

Institutul de Chimie Macromoleculară „Petru Poni" Iaşi

REFEREES: Prof. Univ. Dr. Doina HUMELNICU

Universitatea „Alexandru Ioan Cuza" din Iași, Facultatea de Chimie

Prof. Univ. Dr. Ing. Igor CREȚESCU

Universitatea Tehnică „Gheorghe Asachi" din Iaşi, Facultatea de Inginerie Chimică și Protecția Mediului

CS I Dr. Anton AIRINEI

Institutul de Chimie Macromoleculară "Petru Poni" din Iași, Departamentul de Chimie Fizică a Polimerilor.

In accordance with the Regulation on the organization and conduct of doctoral studies for the awarding of scientific titles within the Romanian Academy, we are sending you the summary of the doctoral thesis and kindly ask you to provide us with your comments and observations. On this occasion, we also invite you to attend the public defense of the doctoral thesis.

Director of PPIMC,

CS I Dr. Valeria HARABAGIU

Tabel of contents

INTRODUCTION

In recent decades, industrialization, urbanization, exponential population growth, and excessive exploitation of natural resources have caused considerable and irreparable damage to the environment [1]. Water contamination is a persistent global problem, highlighting the need for constant re-evaluation of water resource management policies to combat this challenge [7]. Inadequate wastewater management affects both aquatic and terrestrial ecosystems, disrupting ecological balance and endangering biodiversity. This highlights the importance of using innovative technologies to support sustainable industrial development and protect the environment in the industrial sector [10]. Therefore, to combat this problem globally, there is a need to develop advanced, environmentally friendly, affordable, and efficient methods for wastewater treatment [11].

The doctoral thesis entitled "Polymer Nanocomposites with (Photo)catalytic Properties" aims to develop innovative nanocomposite materials with superior photodegradative properties compared to spinel-structured ferrite nanoparticles. These metal oxides have certain advantages, including a large contact surface, high absorption capacity for organic pollutants, and easy recovery from the reaction environment due to their magnetic nature. Thus, a promising new direction for improving the performance of inorganic photocatalysts is the design of composite materials by embedding them in polymer matrices. The polymer material actively participates in improving the photocatalytic and absorption process of organic pollutants because it has a larger contact surface than inorganic nanoparticles.

The topic of the doctoral thesis is of interest in the field of decontamination of micropollutants from water sources. It involves the synthesis and characterization of doped mixed ferrite nanomaterials and the incorporation of these nanoparticles into polymer matrices to obtain nanocomposites with improved photocatalytic properties.

The thesis is divided into two well-defined sections, each targeting precise and well-founded objectives. The first part of the thesis, presented in **Chapter 1**, presents a detailed literature review on wastewater treatment methods, with a focus on the photocatalysis process, photocatalysts and their specific properties, as well as spinel ferrite nanocomposites and various supports used. Next, the second part of the thesis, specifically Chapters 2, 3, and 4, includes personal contributions resulting from the preparation, characterization, and optimization of spinel nanostructures and polymer nanocomposites for (photo)catalytic applications. This feature will allow the production of photocatalysts with superior

properties. **Chapter 2** is dedicated to the materials used, addressing the preparation of two series of spinel ferrites, as well as three series of composite materials based on polyvinylidene fluoride, carboxymethylcellulose with surfactants, and carboxymethylcellulose. At the same time, the chapter details the characterization methods applied for the analysis of nanocomposites.

Subchapter 3.1 addresses the study of undoped and samarium-doped zinc ferrite-based nanomaterials obtained by the sol-gel self-combustion technique. This part discusses the preparation method, characterization, and evaluation of the influence of experimental parameters on the photocatalytic properties in the degradation of organic compounds.

Subchapter 3.2 details the development of new electrophiled nanocomposites obtained by embedding the samarium-doped zinc and aluminum ferrite photocatalyst in a polyvinylidene fluoride matrix. The study focuses on the electrophilation method, the characterization of electrophiled nanocomposites, and their evaluation for photocatalytic applications in the visible range.

Subchapter 4.1 describes the preparation and characterization of manganese-based spinel ferrites with improved properties through the use of rare earth element doping. The applicability of these spinel nanostructures in wet hydrogen peroxide catalysis applications for the degradation of azoic pollutants is then evaluated.

Subchapter 4.2 details the method of obtaining nanocomposites with spherical morphology based on carboxymethyl cellulose, manganese ferrites, and surfactants. The influence of surfactants on the development of nanocomposite materials is investigated. The study also continues with the determination of the adsorption capacity of innovative nanocomposites using organic pollutants.

Subchapter 4.3 presents the method for obtaining nanocomposites with morphology based on carboxymethyl cellulose and undoped and doped manganese ferrites. Next, aspects related to testing the photocatalytic properties on organic pollutants, recovery, and reuse of hydrogel nanocomposites are discussed.

The last part of the thesis is dedicated to the conclusions specific to each chapter, followed by general conclusions and bibliographical references. In addition, the appendices include supplementary material from the experimental chapters (**Appendix** 1), scientific activity carried out (**Appendix 2),** and relevant published works that support the thesis topic (**Appendix 3**).

The thesis summary presents the most significant results achieved. Schemes, figures, tables, and references retain the numbering used in the thesis.

PART II: ORIGINAL CONTRIBUTIONS

The **aim** of this doctoral thesis is to develop polymeric nanocomposite materials with properties that make them suitable for (photo)catalytic applications in the field of depollution of water contaminated with various organic compounds.

In order to achieve the aim of this thesis, a series of specific objectives were taken into consideration.

Specific objectives

O1. Development of syntheses of inorganic materials from the category of mixed oxides with structural, dimensional, and magnetic properties suitable for use in obtaining nanocomposites

- Obtaining Zn-based spinel ferrites substituted with Al and doped with Sm and Mn ferrites doped with La, Ce, Gd, and Er;
- Structural, morphological, textural, and magnetic evaluation of oxide materials;
- Investigation of (photo)catalytic properties in the oxidation processes of recalcitrant organic pollutants and optimization of (photo)catalytic processes;

O2. Development of polymeric nanocomposites based on synthetic and natural polymers and their evaluation in various wastewater depollution processes

- Incorporation of spinel-type ferrite nanoparticles into synthetic (PVDF) or natural (carboxymethylcellulose) polymer matrices;
- Characterization of composites from a morphological, magnetic, mechanical, and textural point of view;
- Evaluation of the adsorption capacity of carboxymethylcellulose granules;
- Investigation of the depollution capabilities of the prepared polymer composites, alongside the elucidation of the mechanisms responsible for their activity.

CHAPTER 3. POLYMERIC NANOCOMPOSITES BASED ON MODIFIED ZINC FERRITES

3.1. Zn and Al spinel ferrites with photocatalytic properties

3.1.1. Introduction

The aim of this subsection is to investigate the properties of zinc ferrites resulting from the substitution of Fe^{3+} cations with Al^{3+} and from doping with a representative rare-earth element, namely samarium. Thus, in the present work, ternary spinel ferrites with the general formula $ZnAlFe_{1-x}Sm_xO_4$ (x = 0; 0.02; 0.04; 0.06; 0.08), were obtained and evaluated for the first time, serving as efficient photocatalysts for the removal of the Evans Blue dye from synthetic wastewater under UV-Vis irradiation.

3.1.2. Preparation of zinc- and aluminum-based spinel ferrites, undoped and samarium-doped

The sol–gel auto-combustion method was used to synthesize aluminum-substituted and samarium-doped zinc ferrites with the general formula $ZnAlFe_{1-x}Sm_xO_4$ (x = 0,02; 0,04; 0,06; 0,08) [124, 247]. The synthesis was carried out in several stages: formation of the gel from metal precursor solutions mediated by citric acid, auto-combustion (dehydration accompanied by the formation of oxide particles), and completion of the ferrite structure through thermal treatments involving pre-sintering and sintering. A graphical representation of the process leading to the final products is shown in **Scheme 2.1**.

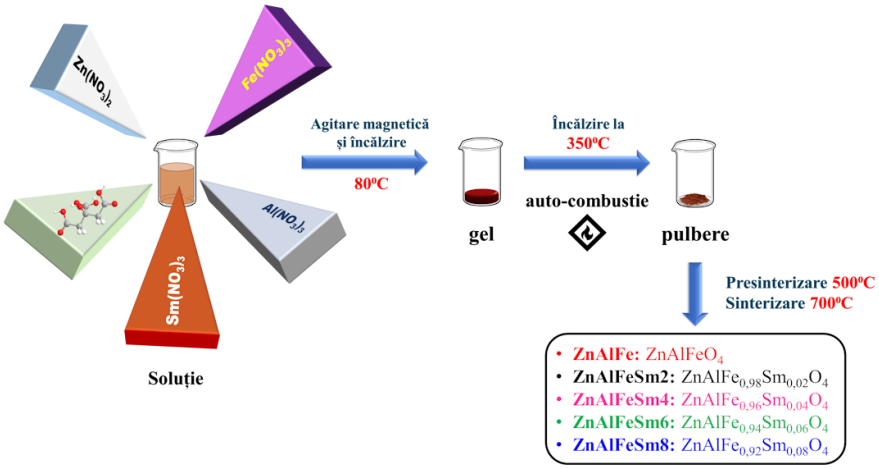

Scheme 2.1. *Synthesis steps for the photocatalysts with the general formula $ZnAlFe_{1-x}Sm_xO_4$ (x = 0; 0.02; 0.04; 0.06; 0.08)*

3.1.3.1. Structural analysis by X-ray diffraction

The crystalline structure of the synthesized ferrite samples was evidenced by wide-angle X-ray diffraction (XRD). The diffractograms recorded for the ferrite samples in

powder form are shown in **Figure 3.1**, while the chemical formulas, sample codes, and calculated data are presented in **Tabel 3.4**.

The results obtained from indexing the diffractograms, using zinc ferrite as referenced in JCPDS card no. 22-1012 [272, 273], revealed the exclusive presence of the characteristic diffraction planes: (220), (311), (222), (400), (422), (511), (440), (620) and (533). These indicate the formation of a pure cubic spinel structure without impurities, confirming the effectiveness of the synthesis method applied for incorporating aluminum and samarium cations into the crystalline structure of the substituted zinc ferrite [274].

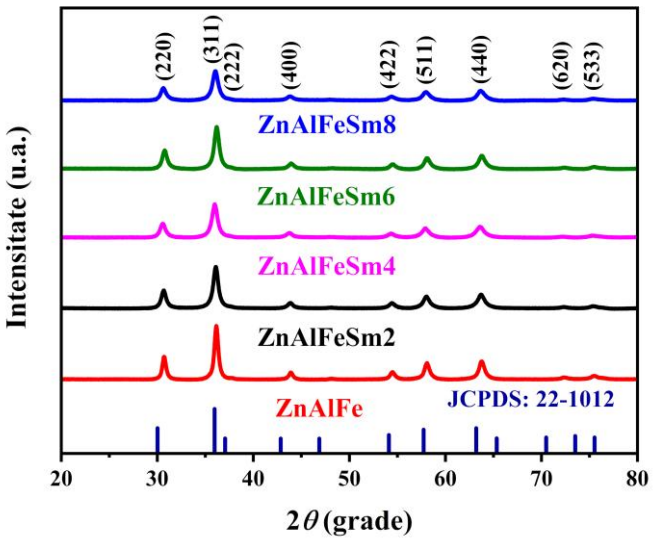

Figure 3.1. *Diffractograms of the undoped ferrite (ZFA) and the samarium-doped ferrites (ZnAlFeSmx); with the general formula: $ZnAlFe_{1-x}Sm_xO_4$ (x = 0; 0.02; 0.04; 0.06; 0.08)) compared with the JCPDS standard nr. 22-1012 [247]*

Based on the processing of the experimental data, the average crystallite sizes (D_{DS}), were determined by using the Debye–Scherrer equation. Additionally, the lattice parameter (a) and the interplanar spacing (d_{311}) were calculated using the Laue and Bragg equations corresponding to cubic crystal lattices.

Table 3.1. *Structural parameters of the undoped and Sm-doped ZnAlFe ferrites calculated from the XRD experimental data*

Chemical formula	**Sample code**	**D_{Ds} (nm)^{XRD}**	**a (Å)^{XRD}**	**d_{311} (Å)^{XRD}**	**$\bar{d}$ (nm)^{TEM}**
$ZnAlFeO_4$	ZnAlFe	13.00	8.2403	1.8423	26.6
$ZnAlFe_{0.98}Sm_{0.02}O_4$	ZnAlFeSm2	11.17	8.2501	1.8446	22.9
$ZnAlFe_{0.96}Sm_{0.04}O_4$	ZnAlFeSm4	10.34	8.2457	1.8434	20.9
$ZnAlFe_{0.94}Sm_{0.06}O_4$	ZnAlFeSm6	10.26	8.2359	1.8410	17.3
$ZnAlFe_{0.92}Sm_{0.08}O_4$	ZnAlFeSm8	10.04	8.2525	1.8453	19.4

In this context, an increase is observed in both the lattice parameter a and the interplanar spacings for the Sm-containing materials, with the exception of the **ZnAlFeSm6** sample. Nevertheless, the amount of rare-earth element incorporated and the calculated

structural parameters indicate that the redistribution of Zn, Fe, and Al cations between the tetrahedral and octahedral sites is governed primarily by the presence of Sm ions. [275, 276].

3.1.3.3. Morphological analysis by transmission electron microscopy

The morphology of the obtained particles was investigated by transmission electron microscopy (TEM).

The recorded images and the particle size distribution are shown in **Figure 3.3** [247]. TEM analysis reveals a significant decrease in the average particle size and a narrowing of the particle size distribution in the case of the doped ferrites, supporting the observations from the XRD analysis. This study confirmed that all analyzed materials fall within the nanometric range, exhibiting a narrow distribution and a low tendency toward agglomeration. Owing to these properties, the **ZnAlFeSm6** sample, which displayed the smallest crystallite and particle sizes, was selected for the preparation of composite photocatalytic membranes, presented in detail in **Subchapter 3.2**.

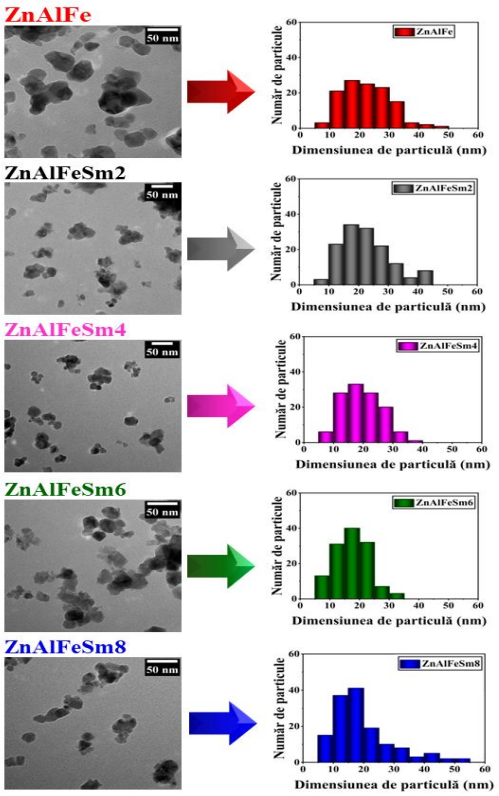

Figure 3.3. *Representative TEM micrographs and particle size distributions of the spinel ferrite nanoparticles* [247]

.

3.1.4. Evaluation of photocatalytic properties

3.1.4.1. Efficiency of spinel ferrites in the photodegradation of Evans Blue (EB)

The photocatalytic activity of the spinel-type compounds $ZnAlFe_{1-x}Sm_xO_4$ (x = 0; 0.02; 0.04; 0.06; 0.08) was evaluated by monitoring the degradation of the pollutant Evans Blue at room temperature under UV irradiation. Evans Blue (EB) was selected as the model organic pollutant due to its widespread use in various fields—such as medicine, food processing, and textile dyeing—as well as its high toxicity to the human organism [285, 286].

The recorded absorption spectra of the EB degradation process, in the presence of the spinel-structured photocatalysts, are shown in **Figure 3.7a–e**. The efficiency of the photocatalysts in degrading the dye molecules is evidenced by the decrease in the intensity of the absorption bands with maxima at 320 and 606 nm, respectively.

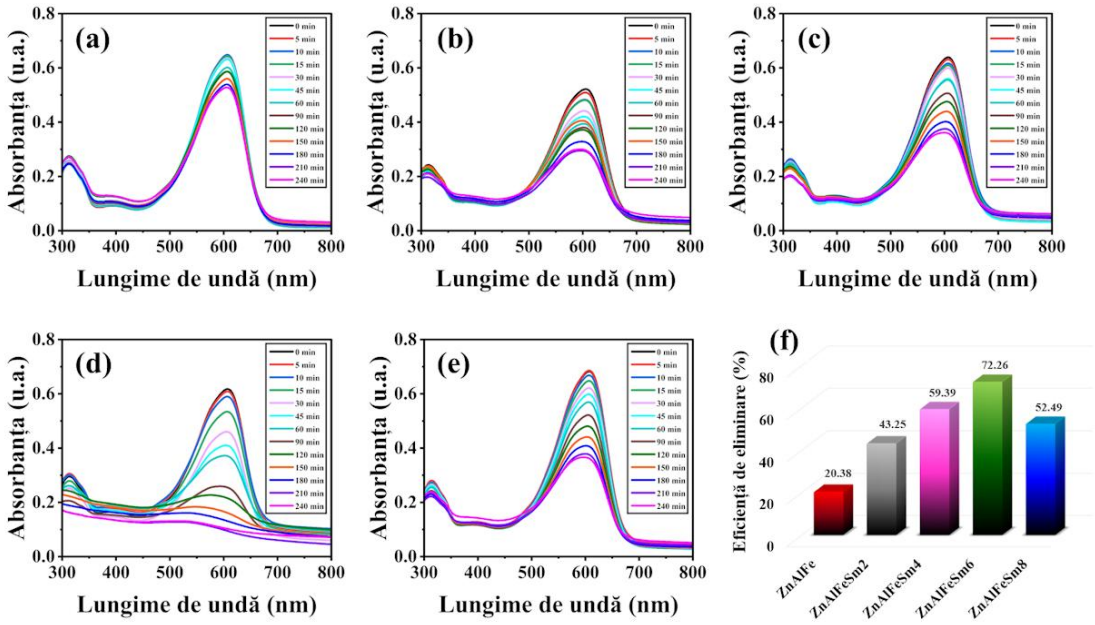

Figure 3.7. *Absorption spectra of the EB pollutant during the photodegradation process using (a) $ZnAlFeO_4$, (b) $ZnAlFe_{0,98}Sm_{0,02}O_4$, (c) $ZnAlFe_{0,96}Sm_{0,02}O_4$, (d) $ZnAlFe_{0,94}Sm_{0,06}O_4$, (e) $ZnAlFe_{0,92}Sm_{0,08}O_4$, and (f) the dye degradation efficiency after one hour [247]*

The photodegradation efficiency of the five spinel materials was assessed by monitoring the degradation of Evans Blue (EB) over a one hour period (**Figure f**). All Sm^{3+}-doped photocatalysts exhibited higher decolorization efficiency compared to the undoped sample (**ZnAlFe**). Among the four Sm-doped spinel ferrites, the material displaying the highest performance in the degradation process was $ZnAlFe_{1,94}Sm_{0,06}O_4$ (**ZnAlFeSm6**). The superior photodegradation behavior of the mixed ferrites can be attributed to several structural parameters, namely the lattice parameter, the interplanar spacing, and the particle size (**Table 3.4**).

3.1.4.2. Kinetics of the photocatalytic reaction under UV-Vis irradiation

Figure 3.8 illustrates the kinetic degradation profiles of the EB dye under both photolytic conditions (absence of catalyst) and in the presence of mixed Zn–Al ferrites, either Sm-doped or undoped. The doped ferrites exhibit superior adsorption capacity and a higher EB degradation rate compared to the undoped material, indicating a substantial enhancement of their photocatalytic performance. This improvement arises from modifications to the crystal lattice and the dopant-induced reduction in particle size.

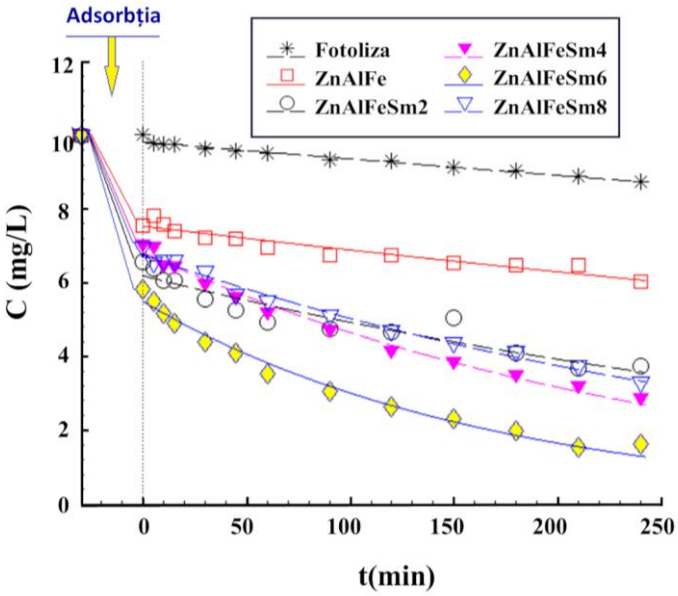

Figure 3.8. *First-order kinetic profiles obtained during the photodegradation of EB using the synthesized photocatalysts (catalyst dose = 0.75 g/L), at 25 °C ± 1 and pH 7.0 ± 0.2, under UV–Vis irradiation [247]*

The photodegradation rate constants calculated from the kinetic data using the pseudo-first-order (PFO) kinetic model are negligible for the photolysis process (k = 4.886 × 10^{-4} min^{-1}), nearly twice as high for the undoped ferrite (k = 8.983 × 10^{-4} min^{-1}), and increase by an order of magnitude for the doped ferrites, with the highest rate recorded for the **ZnAlFeSm6** sample (k = 6.014 × 10^{-3} min^{-1}). The superior photodegradation performance of this material correlates with its lower particle size, reduced lattice parameter, and smaller interplanar spacing. Owing to its enhanced behavior, the **ZnAlFeSm6** sample was selected for the optimization stage of the photodegradation process.

3.1.4.3. Optimization of the photocatalytic process: effect of hydrogen peroxide and catalyst amount

To enhance the performance of EB photodegradation under UV–Vis irradiation, two quantitative parameters were varied: the hydrogen peroxide concentration ($[H_2O_2]$) and catalyst loading (*CatDose*) This approach enabled the assessment of each variable's influence on the system of interest and the determination of the maximum yield, considered the process response to changes in experimental conditions.

By applying the mathematical conversion of the experimental variables into real values, the optimal point of the process was identified, corresponding to a catalyst dosage (CatDose) of 0.765 g/L and a hydrogen peroxide concentration of 0.077 M

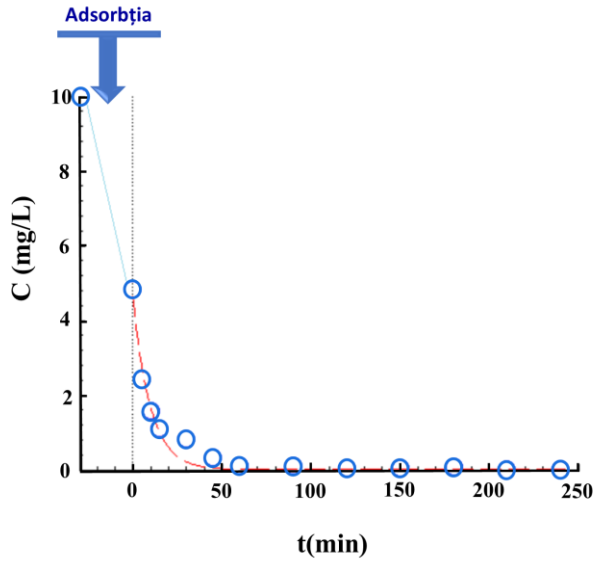

***Figure 3.11**. Kinetics of the photocatalytic degradation of the EB pollutant under UV–Vis irradiation using the ZnAlFeSm6 photocatalyst, under optimal experimental conditions:: t = 25±1°C, CatDose = 0.765 g/L, [H_2O_2]= 0.077 M [247]*

Thus, the experimental validation of the optimization procedure was performed by monitoring the photodegradation kinetics of EB under the optimal concentrations of hydrogen peroxide and catalyst (**Figure 3.11**). Under these optimized conditions, a rate constant of $k = 1.020 \times 10^{-1}$ min^{-1} was obtained, corresponding to a half-life $\left(\tau = \frac{ln2}{k}\right)$ of 7 minutes. Upon completion of the kinetic experiment, conducted over a 4-hour period, complete degradation of the EB pollutant was achieved, with the process yield effectively reaching 100%.

3.2. Nanostructured composite materials based on polyvinylidene fluoride (PVDF) and samarium-doped zinc–aluminum ferrite for pollutant degradation in aqueous solutions

3.2.1. Introduction

In this subsection, innovative PVDF-based hybrid membranes produced via electrospinning were synthesized, characterized, and comprehensively analyzed, and their photocatalytic performance was systematically evaluated. The mixed zinc–aluminum spinel ferrite doped with samarium ($ZnAlFe_{0.94}Sm_{0.06}O_4$) was selected as the inorganic filler owing to its outstanding photocatalytic properties demonstrated in the preceding subsection. Using the electrospinning technique, composite ZnAlFeSm6/PVDF membranes containing 10% and 20% inorganic filler (**10ZnAlFeSm6/PVDF** and **20ZnAlFeSm6/PVDF**) were fabricated. Their structural, morphological, mechanical, textural, and magnetic

characteristics were examined in detail. To assess the photocatalytic efficiency of the **ZnAlFeSm6/PVDF** membranes, Methylene Blue was employed as a representative organic pollutant. Furthermore, the influence of pH was investigated, the reactive species involved were identified through scavenging experiments, and the stability and reusability of the photocatalyst were evaluated, thereby underscoring the potential of these materials for environmental depollution applications

3.2.2. Preparation of composite membranes

"The composite membranes were fabricated via the electrospinning technique, following a multistep protocol that included ferrite dispersion by ultrasonication, homogenization of the dispersed ferrite within the PVDF–PVP (porogenic agent) solution, electrospinning, subsequent water-washing to remove the porogen, and final drying [227]. Two composite membranes containing 10% (**10ZnAlFeSm6/PVDF**) and 20% (**20ZnAlFeSm6/PVDF**) inorganic filler were obtained. For comparative purposes, a pristine **PVDF** membrane was also synthesized as a reference (**Scheme 2.2**).

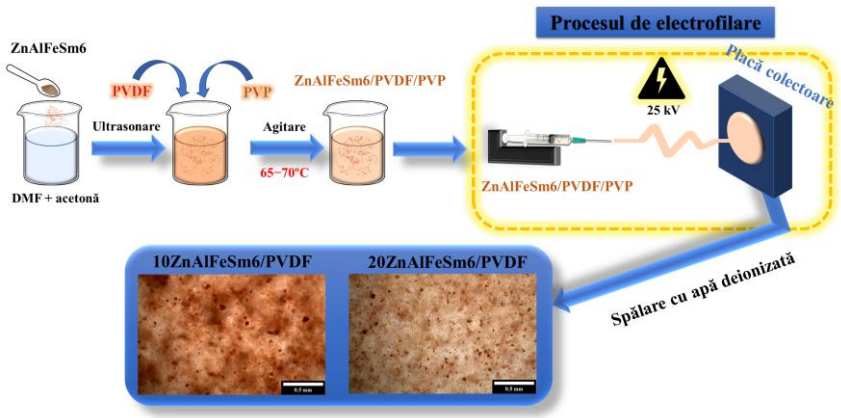

Scheme 2.2. *Synthesis diagram of the 10ZnAlFeSm6/PVDF and 20ZnAlFeSm6/PVDF composite membranes obtained by the electrospinning method3.2.3. Caracterizarea membranelor compozite*

3.2.3.3. Morphological characterization of PVDF-based composites

The morphological characterization of the electrospun membranes was conducted using scanning electron microscopy. The micrographs corresponding to the composite membranes **10ZnAlFeSm6/PVDF** (**Figure 3.14(d,e)**) and **20ZnAlFeSm6/PVDF** (**Figure 3.14(i,j)**) were compared with those of the pristine PVDF membrane (**Figure 3.14(a,b)**). The **PVDF** fibers exhibit uniform, smooth surfaces and an average diameter of 0.64 ± 0.44 μm, with no evidence of compositional agglomeration. In contrast, the composite fibers display similarly smooth morphologies but contain inorganic aggregates on their surfaces, a feature

consistent with observations reported for other electrospun nanocomposite systems [307, 310, 312].

SEM analysis further confirmed that the incorporation of **10%** and **20% ZnAlFeSm6** results in the appearance of surface-bound inorganic clusters, while the overall fiber network remains homogeneous, indicating efficient dispersion of the spinel ferrite within the polymer matrix. All membranes exhibit a porous architecture composed of randomly oriented fibers, a configuration that promotes effective interaction between pollutants and photocatalytically active sites. The introduction of the inorganic phase also led to an increase in fiber diameter.

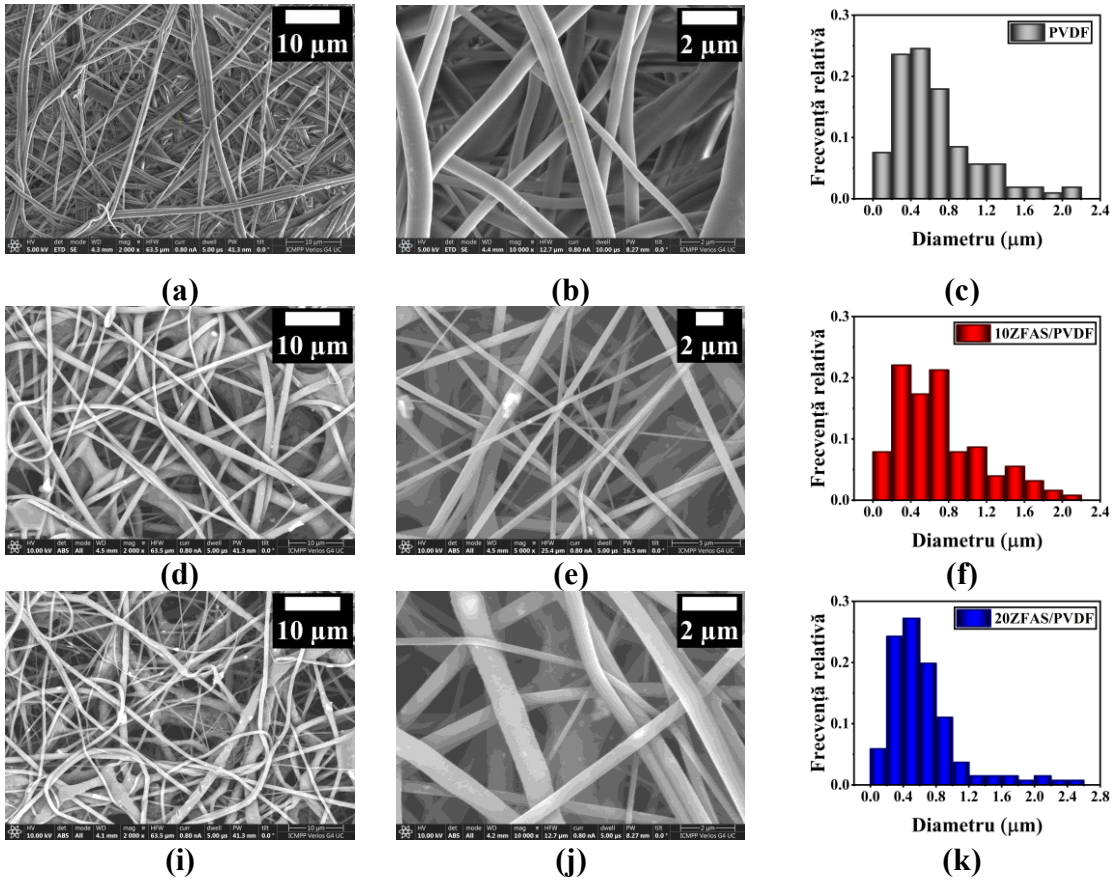

Figure 3.14. *SEM micrographs of: (a, b) PVDF, (d, e), composite material containing 10% ZnAlFeSm6 și (i, j), composites containing 20% ZnAlFeSm6; Fiber diameter distribution histograms for: (c) PVDF; (f) 10ZnAlFeSm6/PVDF and (k) 20ZnAlFeSm6/PVDF composite membranes [227]*

3.2.4. Evaluation of photocatalytic performance (UV-Vis)

The composite membranes (**10ZnAlFeSm6/PVDF** and **20ZnAlFeSm6/PVDF**) were employed to evaluate their photocatalytic performance toward a model pollutant, methylene blue (MB). According to the established protocol [227, 315], a 5 mg/L MB solution was irradiated with a visible-light lamp (400 W) for 600 minutes. The concentration of MB in solution was monitored using a UV–Vis spectrophotometer. For comparison, the absorption spectra of MB were recorded at different irradiation times in the absence of any photocatalyst (photolysis test).

Photolysis experiments resulted in only a 32% decrease in the intensity of the MB absorption band, whereas the use of the composite membranes yielded degradation efficiencies between 80% and 96%, depending on the membrane formulation and catalyst dosage. Adsorption processes accounted for 15.33–30.01% of the overall removal, and the photocatalytic performance was closely associated with membrane porosity, filler loading, and the dispersion quality of the inorganic phase. The highest efficiency (96%) was obtained for the **10ZnAlFeSm6/PVDF** composite at a dosage of **0.5% w/v**, a behavior attributed to its favorable specific surface area and pore architecture, which facilitate efficient mass transfer.

3.2.4.1. Kinetics of MB pollutant photodegradation

In this section, a kinetic analysis of the photodegradation process was conducted to assess the photocatalytic activity of the composite membranes toward methylene blue (MB).

Figure 3.21 presents the experimental kinetic evolution of the pollutant under visible-light irradiation in the presence of the photocatalytic membranes (**10ZnAlFeSm6/PVDF** and **20ZnAlFeSm6/PVDF**).

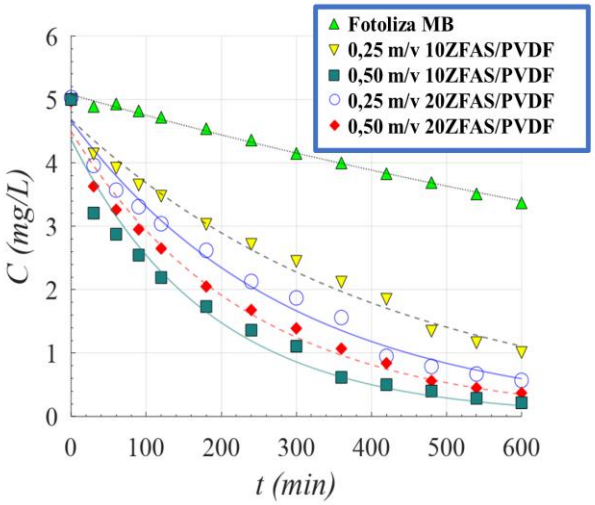

***Figure 3.21**. Photodegradation kinetics of MB under visible-light irradiation in the presence of composite-membrane photocatalysts (10ZnAlFeSm6/PVDF and 20ZnAlFeSm6/PVDF) at T = 25 ± 1 °C and pH = 6.0 ± 0.2; the solid and dashed lines represent the model-estimated response according to the PFO kinetic model [227]*

The agreement between the estimated and experimental data was assessed using the error function (ε^2), defined as the sum of squared residuals ($\varepsilon^2 = \sum(C(t)_{exp} - C(t)_{calc})^2$). A lower value of ε^2 indicates a more accurate fit of the PFO kinetic model. The kinetic parameters calculated for the PFO model are presented in **Table 3.13**. The optimal composite membrane was identified as **10ZnAlFeSm6/PVDF** at a loading of **0,50%** w/v, under which conditions the highest rate constant was obtained (k = 5.413 × 10^{-3} min^{-1}).

***Table 3.2**. Datele experimentale calculate cu ajutorul modelului PFO, pentru fotodegradarea MB, cu ajutorul fotocatalizatorilor polimerici*

Sample code	Photocatalyst dose (% g/100 mL)	k (min^{-1})	Error (ε^2)
--	photolysis	6.689 × 10^{-4}	0.021
10ZnAlFeSm6/PVDF	0.25	2.402 × 10^{-3}	0.301
10ZnAlFeSm6/PVDF	**0.50**	**5.413 × 10^{-3}**	**0.872**
20ZnAlFeSm6/PVDF	0.25	3.428 × 10^{-3}	0.403
20ZnAlFeSm6/PVDF	0.50	4.267 × 10^{-3}	0.438

3.2.4.3. Identification of active species

To clarify the mechanism underlying the photodegradation reaction of the organic pollutant, active-species trapping experiments were conducted using various chemical scavengers [323]. Such scavengers typically inhibit the photodegradation reaction, thereby revealing the predominant reactive species involved in the system.

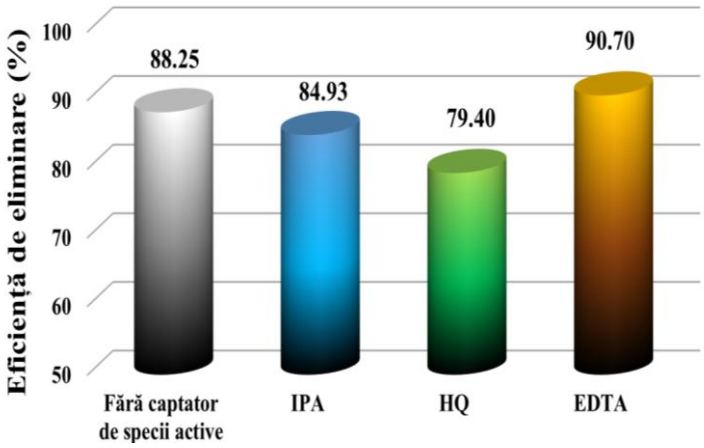

***Figura 3.23.** Influence of scavengers on the photodegradation of MB under visible-light irradiation for 6 hours in the presence of the 10ZnAlFeSm6/PVDF photocatalytic membrane [227]*

In this study, the following scavengers were employed: isopropyl alcohol (IPA) to capture hydroxyl radicals (HO•), hydroquinone (HQ) to trap superoxide radicals (•O_2^-), and ethylenediaminetetraacetic acid (EDTA, used as EDTA-Na) to quench photogenerated holes

(h^+) in the valence band of the inorganic photocatalyst ($ZnAlFe_{0.94}Sm_{0.06}O_4$). All scavengers were used at a concentration of 5 mM.

Figure 3.23 presents the results of the trapping experiments, highlighting the influence of each scavenger on the decolorization efficiency. The presence of EDTA produced no significant effect on the photodegradation process, indicating that valence-band holes (h^+) of the spinel-structured catalyst play a negligible role. In contrast, IPA induced a moderate reduction in photodegradation efficiency, suggesting the partial involvement of hydroxyl radicals (HO•). The most pronounced inhibitory effect was observed in the presence of HQ, where the decolorization efficiency decreased from 88.25% to 79.40%, thereby confirming that the superoxide radical ($•O_2^-$) was the main active species responsible for the photodegradation of MB (**Figure 3.24**).

These findings are fully consistent with recent reports on the photodegradation of organic dyes using composite membranes irradiated under visible light [324].

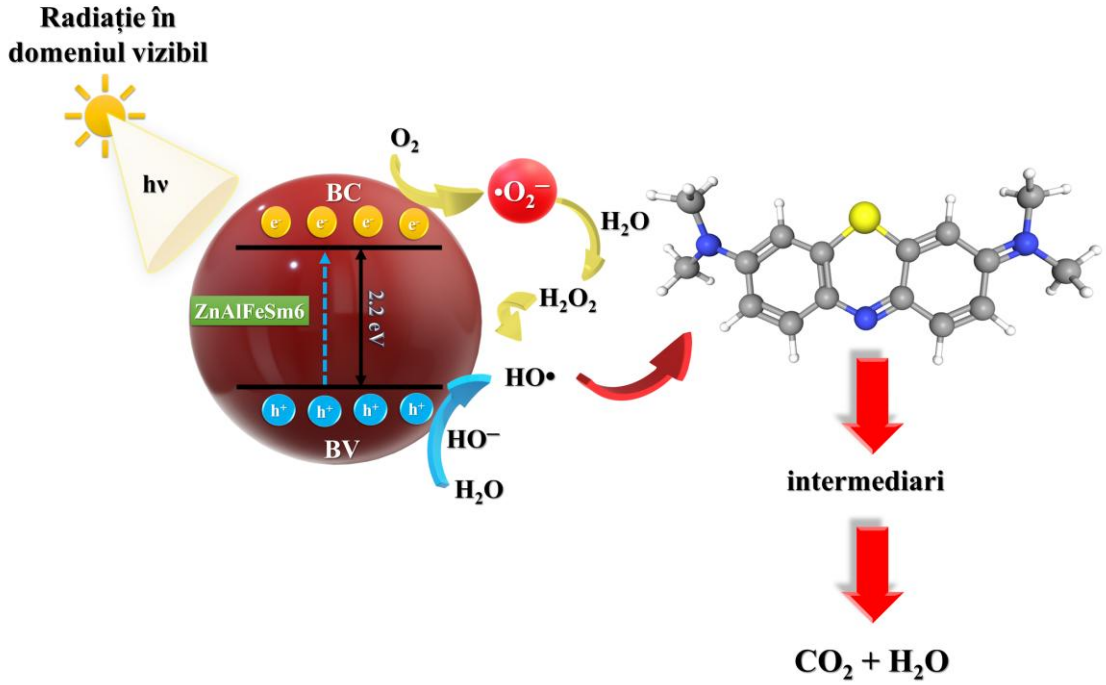

Figure 3.24. *Schematic representation of the photodegradation mechanism of MB in the presence of 10ZAFS/PVDF and the influence of the different scavengers. [227]*

CHAPTER 4. POLYMERIC NANOCOMPOSITES BASED ON MODIFIED MANGANESE FERRITES

4.1. Mn spinel ferrites with catalytic properties

4.1.1. Introduction

This subsection focuses on the synthesis of nanostructured manganese ferrite catalysts doped with rare-earth metals (La^{3+}, Ce^{3+}, Gd^{3+}, Er^{3+}) and their application in the catalytic wet oxidation of organic pollutants using hydrogen peroxide. These materials were investigated in terms of their structural, morphological, textural, and magnetic properties. In addition, their catalytic performance was evaluated for the degradation of the model pollutant Orange II (OII).

4.1.2. Synthesis of manganese ferrites, doped and undoped with rare-earth metals.

Manganese ferrites with the general formula $MnFe_{2-x}RE_xO_4$ (unde, x=0 și 0,04; RE = La, Ce, Gd și respectiv, Er), were synthesized via the sol–gel auto-combustion method [248], using metal nitrates as cation precursors and citric acid as the fuel in a 1:3 molar ratio. The gel formed through precursor complexation at 80 °C was subsequently subjected to thermal treatment at 350 °C, yielding homogeneous black powders characteristic of the spinel phase. Through this procedure, five materials were obtained: the undoped ferrite (**MnFe**) and four 2% rare-earth-doped variants **MnFeLa**, **MnFeCe**, **MnFeGd**, and **MnFeEr** (**Scheme 2.3**).

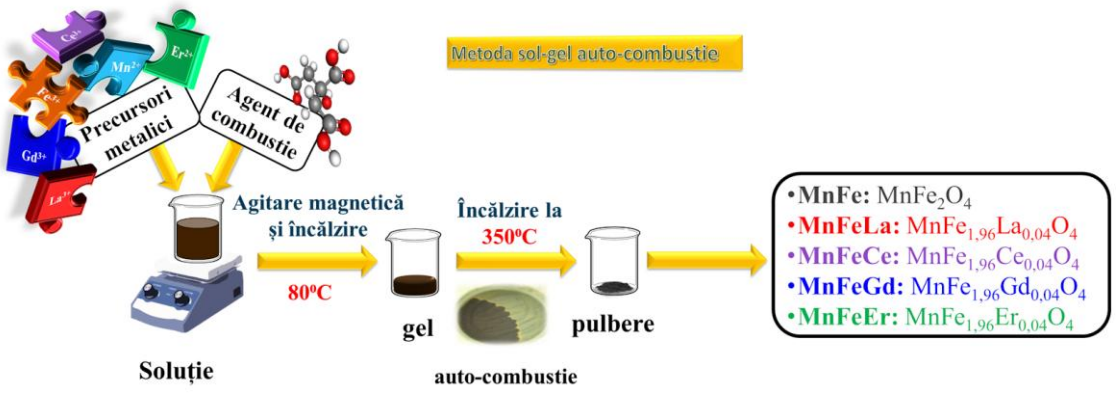

Scheme 2.3. *Schematic representation of the synthesis route for the photocatalysts with the general formula $MnFe_{2-x}RE_xO_4$ (x = 0,04; RE = La, Ce, Gd, Er)*

4.1.3.1. Crystalline structure of spinel ferrites

XRD analysis was employed to investigate the structural properties of the undoped and doped spinel ferrites.

The diffractograms (**Figure 4.1**) show that all synthesized samples exhibit a pure cubic spinel structure. These results confirm that the selected synthesis method successfully enabled the incorporation of rare-earth cations into the spinel lattice of manganese ferrite [274, 352-356].

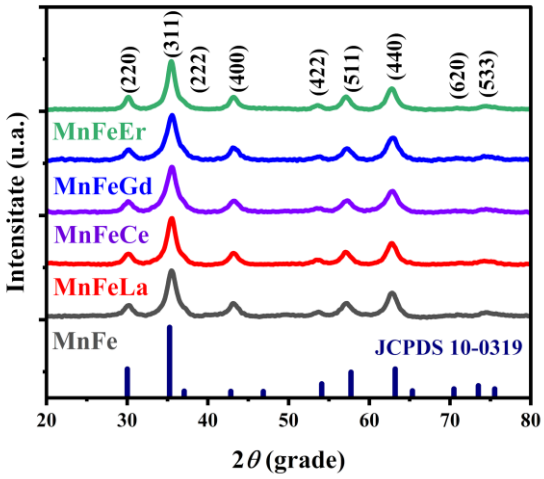

Figura 4.1. *Recorded diffractograms of the five manganese-based spinel ferrites with the general formula $MnFe_{2-x}RE_xO_4$ (x=0; 0,04 and RE = La, Ce, Gd, Er)*

4.1.3.3. Morphological analysis by transmission electron microscopy

TEM analysis (**Figure 4.3**) revealed nanometric particles exhibiting spherical and/or polyhedral morphologies, along with a pronounced tendency toward agglomeration, a behavior characteristic of magnetic materials. Selected-area electron diffraction confirmed the polycrystalline nature of all samples through the presence of well-defined diffraction rings [364, 365]. The average particle sizes determined by TEM were slightly larger than the crystallite sizes estimated by XRD, ranging from 7.1 nm for the undoped ferrite to 5.5–7.4 nm for the doped samples. Among these, **MnFeCe** displayed the smallest particle dimensions, whereas **MnFeLa** exhibited the narrowest size distribution.

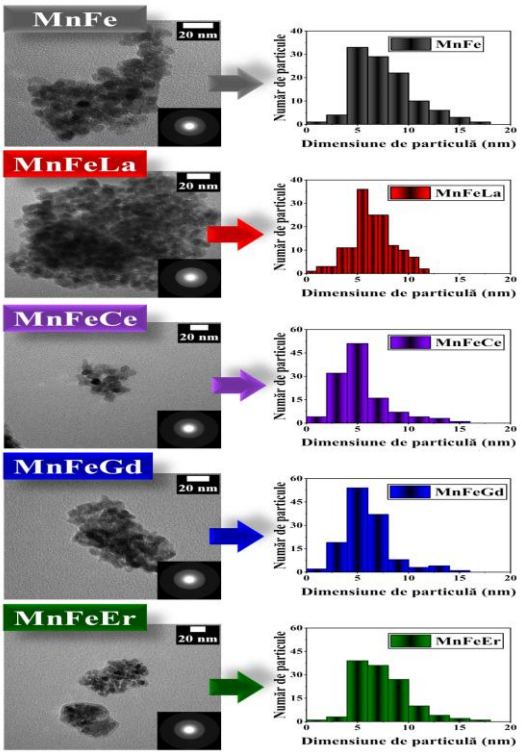

Figura 4.3. *Representative micrographs, selected-area electron diffraction (SAED) patterns (left), and particle size distributions (right) for the **MnFe**, **MnFeLa**, **MnFeCe**, **MnFeGd** and **MnFeEr** samples*

Overall, the TEM analysis confirmed the nanometric particle dimensions, the relatively uniform size distribution, and the characteristic agglomeration behavior of magnetic spinel ferrites

4.1.4. Catalytic wet peroxide oxidation (CWPO) of pollutants in synthetic wastewater

The UV–Vis spectra recorded in the 300–600 nm range exhibited the three characteristic absorption bands of Orange II at 310 nm (naphthalene ring), 400 nm (n–π* transitions of the azo group), and 485 nm (N=N bond) [253]. In the absence of the catalyst, only minimal spectral variations were observed, indicating that the dye remained stable under the reaction conditions. In contrast, in the presence of the spinel ferrites, the intensity of all absorption bands progressively decreased with irradiation time, confirming the degradation of both the aromatic ring and the azo moiety during the CWPO processes

4.1.4.1. Kinetic analysis of CWPO reaction of Orange II

The degradation kinetics of Orange II during the CWPO processes at 333 and 343 K are presented in **Figure 4.7**, and the experimental data were fitted using a pseudo-first-order (PFO) kinetic model through nonlinear regression. The resulting parameters (**Table 4.5**) indicate that at 343 K all catalysts exhibited rate constants on the order of 10^{-1} min^{-1} and achieved more than 97% decolorization within the first 30 minutes. The undoped $MnFe_2O_4$ catalyst displayed the highest activity, reaching a PFO rate constant of 2.068×10^{-1} min^{-1}.

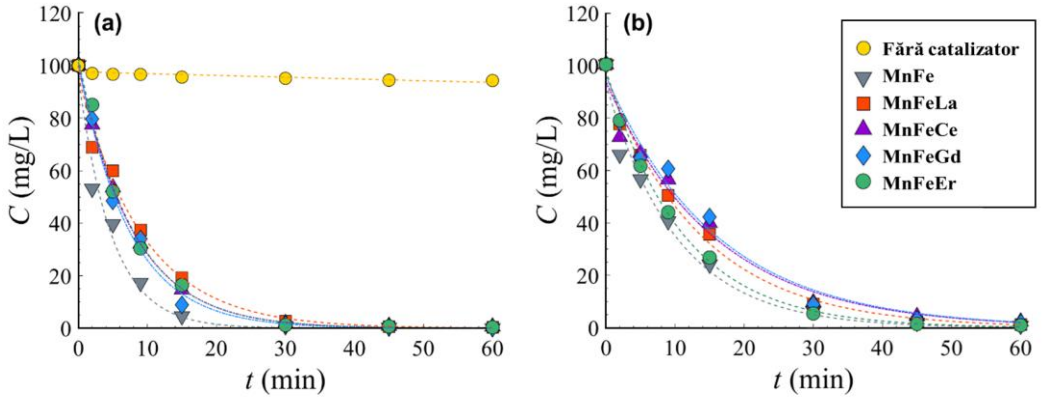

Figure 4.7. *Kinetic curves corresponding to the degradation of Orange II in the presence of the manganese ferrite–based catalysts; the dotted lines represent the model predictions according to the PFO kinetic model. Experimental conditions: catalyst concentration = 0,5 g/L; T = 60-70 ± 1 °C ; pH 3,0 ± 0,1; concentrație de H_2O_2 = 0,1M*

Among the doped catalysts, $MnFe_{1,96}Gd_{0,04}O_4$ (**MnFeGd**) exhibited the best catalytic performance, with a rate constant of 1.364×10^{-1} min^{-1}. For the CWPO processes carried out at lower temperatures (333 K and 323 K), the observed PFO rate constants were on the order

of 10^{-2} min^{-1}, indicating a reduced reaction intensity, particularly at 323 K. The activation energy (E_a, kJ×mol^{-1}) was determined from Arrhenius plots (ln k vs. 1/T), based on the temperature-dependent PFO rate constants (**Table 4.5**).

Table 4.5. *Kinetic parameters of the wet catalytic oxidation of Orange II in the presence of the spinel-structured catalysts*

Catalyst	**Formula chimică**	***k* (min^{-1}) at 343 K**	***k* (min^{-1}) at 333K**	***k* (min^{-1}) at 323K**	***Ea* (kJ/mol)**
No catalyst	-	7.105×10^{-4}	-	-	-
MnFe	$MnFe_2O_4$	2.068×10^{-1}	9.733×10^{-2}	4.478×10^{-2}	70.45
MnFeLa	$MnFe_{1.96}La_{0.04}O_4$	1.073×10^{-1}	7.315×10^{-2}	3.039×10^{-2}	58.35
MnFeCe	$MnFe_{1.96}Ce_{0.04}O_4$	1.263×10^{-1}	6.390×10^{-2}	3.858×10^{-2}	54.53
MnFeGd	$MnFe_{1.96}Gd_{0.04}O_4$	1.364×10^{-1}	6.310×10^{-2}	4.087×10^{-2}	55.34
MnFeEr	$MnFe_{1.96}Er_{0.04}O_4$	1.281×10^{-1}	9.073×10^{-2}	4.234×10^{-2}	51.17

The undoped sample ($MnFe_2O_4$) exibited a 70.45 kJ/mol activation energy. whereas the rare-earth-doped samples exhibited markedly lower values, ranging from 51.17 to 58.35 kJ mol^{-1}.The lowest activation value (51.17 kJ mol^{-1}) was obtained for the erbium-doped manganese ferrite ($MnFe_{1.96}Er_{0.04}O_4$).

The assessment of mineralization by TOC analysis (**Figure 4.8**) after a 4-hour experiment period, indicated efficiencies ranging from 46.65% to 70.60%. The highest degree of mineralization was again achieved by the erbium-doped sample, which outperformed the undoped catalyst. The mineralization trend followed the same order as the magnetic properties of the materials (**MnFeEr** > **MnFeLa** > **MnFeCe** > **MnFeGd**).

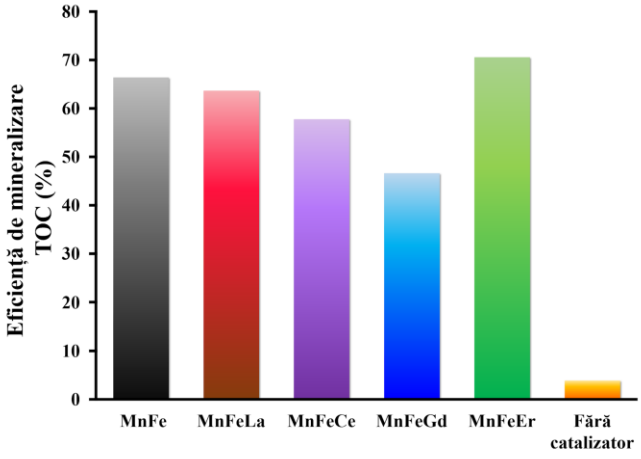

Figura 4.8. *Outcomes of TOC removal efficiency for Orange II dye mineralization in the precence of manganese ferrite-based catalysts, after a 4 hour contact time*

These findings are consistent with literature reports indicating a direct relationship between the magnetic properties of spinel ferrites and their catalytic activity [370].

4.2. Polymeric nanocomposites based on carboxymethylcellulose and manganese ferrites synthesized in the presence of surfactants

4.2.1. Introduction

This subchapter addresses the integration of manganese ferrite nanoparticles into carboxymethylcellulose matrices to obtain advanced nanocomposites exhibiting magnetic, sorptive, and photocatalytic properties. The employed synthesis routes and characterization techniques (FT-IR, XRD, SEM, and VSM) are detailed, emphasizing the structural features and physicochemical behavior of the resulting materials. Sorptive and photocatalytic performances were assessed using representative pollutants, while process monitoring was conducted via UV-Vis spectroscopy, enabling a comprehensive quantitative and qualitative evaluation of the nanocomposites' decoloration efficiency.

4.2.2. Synthesis of carboxymethylcellulose/manganese-ferrite based composites

The synthesis of the carboxymethyl cellulose (CMC)-based composites involved the preparation of a CMC stock solution, followed by the ultrasonication-assisted dispersion of manganese ferrite nanoparticles. Subsequently, the surfactant (SDS) and NaCl were introduced to facilitate the development of porous structures. The resulting mixture was then added dropwise into a $Fe(NO_3)_3$ solution, where ionotropic gelation occurred through the interaction of Fe^{3+} ions with the functional groups of CMC, yielding granules that were subsequently washed and lyophilized.

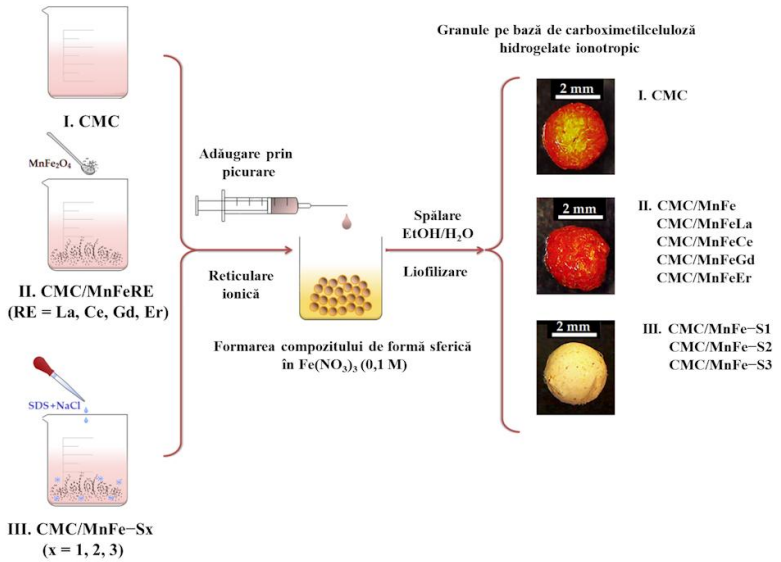

Scheme 2.4. *Schematic representation of the preparation process for the spherical carboxymethylcellulose-based composites, where CMC denotes the 3% carboxymethylcellulose solution (I);* ***CMC/MnFe, CMC/MnFeLa, CMC/MnFeCe, CMC/MnFeGd, CMC/MnFeEr*** *correspond to the dispersions of manganese-based spinel ferrites ($MnFe_2O_4$) in the* ***CMC*** *solution (II); and* ***CMC/MnFe−Sx (x=1, 2, 3)*** *represents the mixture obtained after the addition of SDS to the CMC–manganese ferrite system (III). The resulting granules were named accordingly, reflecting their precursor solutions [249].*

The obtained composites were designated as **CMC/MnFe–S1**, **CMC/MnFe–S2**, and **CMC/MnFe–S3**, according to the CMC:SDS mass ratio. For comparative purposes, additional hydrogels were synthesized either without the magnetic component (**CMC**) or without the surfactant (**CMC/MnFe**, **CMC/MnFeLa**, **CMC/MnFeCe**, **CMC/MnFeGd**, **CMC/MnFeEr**) [249]. A schematic overview of the synthesis process for the CMC-based composites is presented in **Scheme 2.4**.

4.2.3.3. Magnetic characterization of CMC/ferrite composites

The hysteresis loops of the CMC-based composites incorporating $MnFe_2O_4$ (**Figure 4.13**) displayed the characteristic superparamagnetic behavior observed for the pure ferrite, evidenced by negligible coercivity and remanence. The saturation magnetization decreased substantially from 28.8 emu/g for $MnFe_2O_4$ to 1.2–2.1 emu/g for the composites, a consequence of the reduced ferrite content (10%). The incorporation of SDS further diminished the magnetization in proportion to the amount introduced, with the exception of the **CMC/MnFe–S2** sample, which exhibited a comparatively higher magnetization value, an effect attributed to the more efficient dispersion of the magnetic nanoparticles within the polymer matrix. The magnetization values obtained are sufficient to enable the effective separation of the granules from solution under an external magnetic field, even in the presence of adsorbed pollutants. This behavior is illustrated in the image inserted in the lower-right corner of **Figure 4.13**.

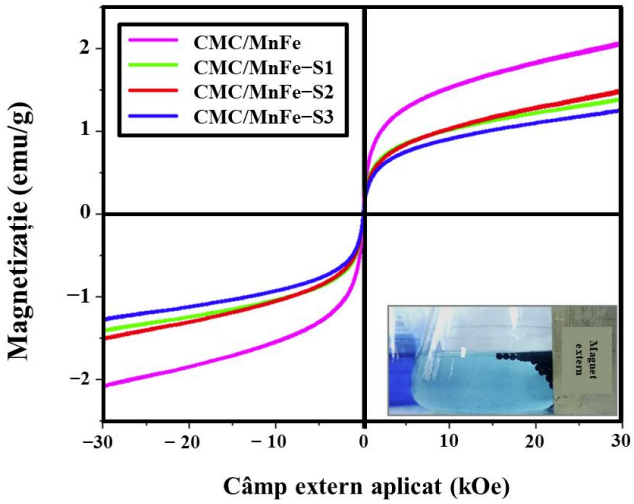

Figura 4.13. *Hysteresis curves of the carboxymethylcellulose granules loaded with manganese ferrite, and magnetic separation of the CMC spheres following the adsorption experiments in an aqueous MB solution, performed under an applied external magnetic field (insert) [249]*

4.3. Polymeric nanocomposites based on carboxymethylcellulose and manganese ferrites with photocatalytic properties

4.3.2. Synthesis of carboxymethylcellulose/manganese-ferrite based composites

The procedure for obtaining the carboxymethyl cellulose-based composites follows a methodology analogous to that described in Subsection 4.2.2 (**Scheme 2.4**).

4.3.3.2. Morphological characterization of CMC-based granules

Morphological analysis of both the cross-sections and surfaces of the carboxymethylcellulose composites investigated in this study was performed by scanning electron microscopy (SEM), as shown in **Figure 4.20**.

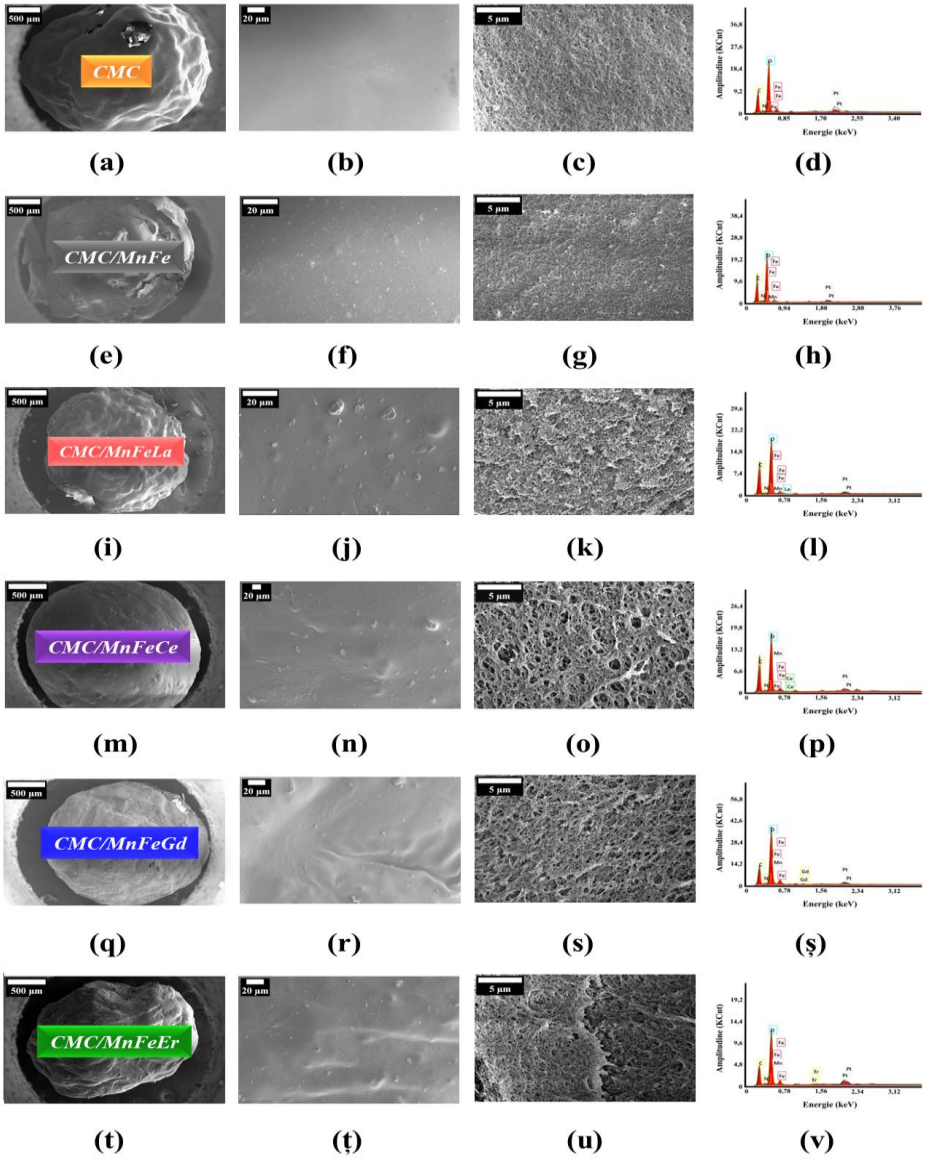

Figure 4.20. *Surface and cross-section micrographs, along with representative elemental analysis images, for the following composites:* ***CMC*** *(a-d),* ***CMC/MnFe*** *(e-h),* ***CMC/MnFeLa*** *(i- l),* ***CMC/MnFeCe*** *(m-p),* ***CMC/MnFeGd*** *(q-ş) and* ***CMC/MnFeEr*** *(t-v)*

Representative surface micrographs in **Figure 4.20(a, b)** correspond to the unmodified carboxymethyl cellulose (**CMC**) matrix and reveal a smooth surface resulting from crosslinking with Fe^{3+} ions. Upon incorporation of undoped (**Figure 4.20e, f**) and doped ferrite nanoparticles (**Figure 4.20i, j, m, n, q, r, t, ț**), the cellulose microfibrils facilitated a uniform dispersion of the magnetic phase across the composite surface. All samples exhibited a spherical morphology (**Figure 4.20e, i, m, q, t**), accompanied by visible agglomerations of the inorganic component **(Figure 4.20f, j, n, r, ț**).

Cross-sectional SEM images recorded at various magnifications (**Figure 4.20c, g, k, o, s** and **u**) revealed a micrometric porous morphology characteristic of lyophilized CMC-based composites, with a homogeneous distribution of the inorganic phase throughout the polysaccharide layers [249]. The incorporation of nanometric inorganic particles into the polysaccharide network resulted in a reduction in granule size—from 2.69 mm for **CMC** to 1.89–2.08 mm for the **CMC/ferrite** composites, an effect attributed to the magnetic interactions of the spinel ferrites, which promote additional compaction during gelation. These observations confirm the successful incorporation of spinel ferrites into the polymer matrix, ensuring a uniform distribution of the inorganic phase within the investigated composite structures.

4.3.4. Evaluation of photocatalytic properties of undoped and doped manganese ferrites embedded in CMC (UV-Vis)

The photodegradation properties of the newly synthesized composite-type catalysts were evaluated using Methylene Blue (MB) as a model pollutant. The pollutant solution, with an initial concentration of 10 mg/L, was irradiated with a UV-domain lamp for 240 minutes. The absorption spectra recorded in the 300–800 nm range are presented in **Figure 4.23**. For comparison, a photolysis experiment of the MB dye in the absence of any photocatalyst was also performed (**Figure 4.23a**)

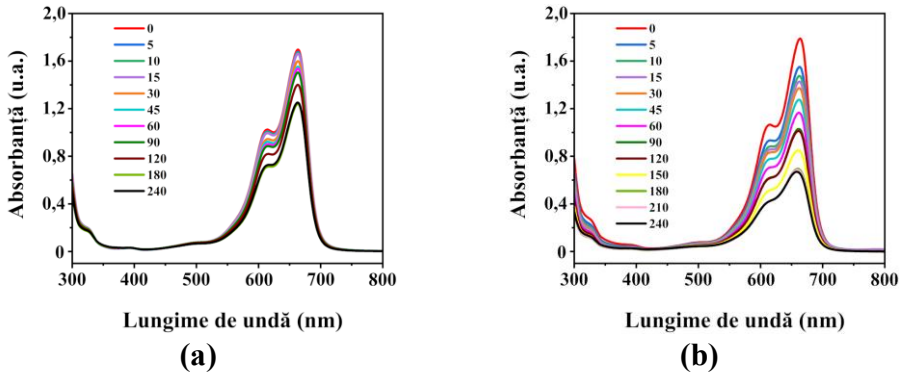

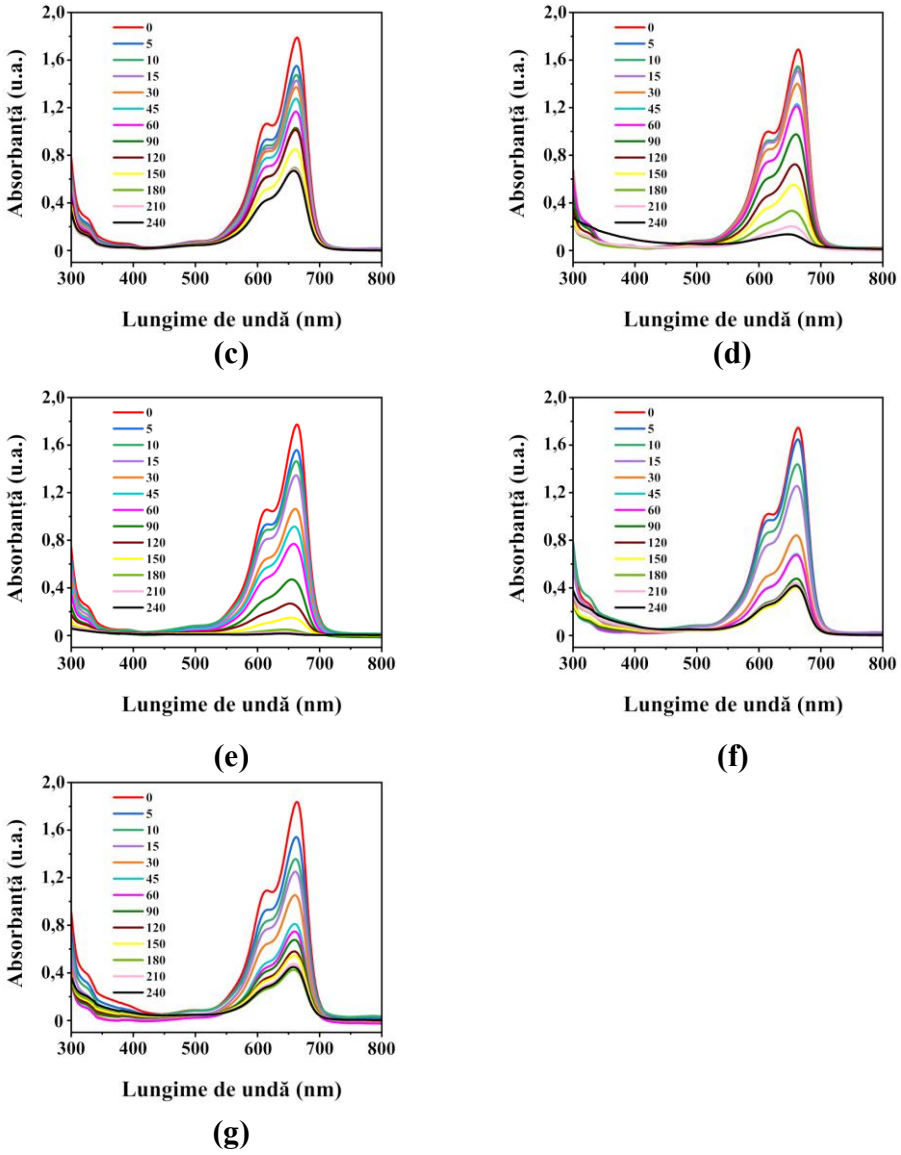

Figure 4.23. *Graphical representation of the evolution of the MB photodegradation process for* ***a) photolysis, b) CMC, c) CMC/MnFe, d) CMC/MnFeLa, e) CMC/MnFeCe, f) CMC/MnFeGd,*** *and* ***g) CMC/MnFeEr***

The progressive decrease in the intensity of the characteristic MB absorption maximum at 664 nm was directly correlated with the increase in reaction time. In the blank experiment, under irradiation with the UV–Vis lamp alone, the MB absorbance decreased by 26.1%, indicating only partial photolysis. In contrast, the catalysts investigated exhibited markedly higher photodegradation efficiencies, with values ranging from 63.5% to 99.3%. Among them, the **CMC/MnFeCe** composite demonstrated the highest performance, achieving a degradation efficiency of 99.3% for the MB dye present in the system.

4.3.4.1. Photodegradation kinetics of MB pollutant

The kinetics of MB photodegradation under UV-Vis irradiation were assessed using the pseudo-first-order model, consistent with standard practice in heterogeneous catalysis.

Figure 4.24 highlights the enhancement of photocatalytic activity achieved through the incorporation of spinel ferrites into the CMC matrix, with the CMC/MnFeCe composite exhibiting the highest performance, reaching a photodegradation efficiency of approximately 100%. Photolysis of MB in the absence of a catalyst was negligible, thereby confirming the essential role of the composites in enabling the advanced oxidation process.

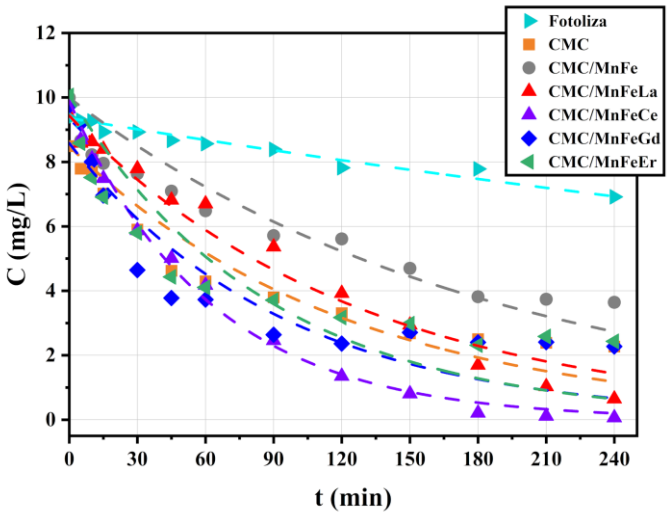

Figura 4.24. *Kinetics of MB photodegradation under visible-light irradiation were investigated in the presence of the synthesized spherical composites, at.t=25±1° C and pH=7,0±0,2*

To validate the applied kinetic model (PFO), a correlation was established between the experimental data and the theoretically estimated values. This correlation enabled the assessment of the model's fidelity and provided relevant insights into the statistical errors associated with the analyzed system. A key indicator in this regard is the mean squared error (ε^2), whose low value reflects the high predictive capability of the model. The experimentally determined parameters corresponding to the PFO model are presented in **Table 4.12**.

Table 4.12. *Experimental parameters derived from the PFO kinetic model for MB photodegradation in the presence of the photocatalysts*

Sample code	**$m_{catalyst}$ (g/600 mL)**	***k* (min^{-1}) ***	**(ε^2)**	**$\tau_{1/2}$ (min^{-1}) ****
--	MB photolysis	1.1171×10^{-3}	0.2195	591.9
CMC	0.25	7.1157×10^{-3}	3.9438	97.4
CMC/MnFe	0.25	4.2968×10^{-3}	2.1941	161.3
CMC/MnFeLa	0.25	7.9775×10^{-3}	3.1770	86.9
CMC/MnFeCe	**0.25**	$\mathbf{1.5634 \times 10^{-2}}$	**0.6650**	**44.3**
CMC/MnFeGd	0.25	1.0645×10^{-2}	15.6890	65.1
CMC/MnFEr	0.25	7.9964×10^{-3}	10.1560	86.7

**k – pseudo-first-order rate constant, **$\tau_{1/2}$ – half life*

The experimental results showed that the synthesized composite materials exhibited rate constants substantially higher than that obtained for the photolysis process. These findings confirm the beneficial influence of rare-earth cations on the photocatalytic performance of the composites. Among all tested materials, the **CMC/MnFeCe** composite displayed the highest rate constant (k = 1,5634 × 10^{-2} min^{-1}) and the shortest half-life ($\tau_{1/2}$ = 44.3 min), indicating superior photocatalytic efficiency. This enhanced performance can be attributed to nanostructural factors such as crystallographic parameters and particle size, which directly govern photocatalytic behavior. Additionally, the uniform dispersion of the inorganic phase, the increased porosity of the materials, and the presence of surface agglomerates contributed to the improved photocatalytic degradation of MB.

CHAPTER 5. GENERAL CONCLUSIONS

The original contributions presented in the doctoral thesis entitled "Polymeric Nanocomposites with Photocatalytic Properties" enabled the formulation of the following general conclusions for each chapter:

Chapter 3

In this subsection, new aluminum-substituted zinc ferrites, both undoped and samarium-doped ($ZnAlFe_{1-x}Sm_xO_4$, x = 0; 0.02; 0.04; 0.06; 0.08), were synthesized using the sol–gel auto-combustion method, which effectively facilitated the incorporation of Al and Sm cations into the spinel lattice.

XRD analysis confirmed the formation of the spinel phase, while TEM microscopy revealed a progressive reduction in particle size with increasing Sm content.

The photocatalytic performance under UV–Vis irradiation was assessed using Evans Blue dye and the newly obtained spinel ferrites. The nanostructures exhibited superior activity compared to the reference sample, underscoring the crucial role of Sm doping. Catalytic performance correlated strongly with the lattice parameter, interplanar spacing, and particle size, with ZnAlFeSm6 displaying the highest photocatalytic efficiency (72%).

Process optimization was achieved by adjusting the catalyst dosage and the hydrogen peroxide concentration. Based on the calculations, the rate constant under optimal conditions ($k = 1.020 \times 10^{-1}$ min^{-1}) was markedly higher than that obtained under the initial photodegradation conditions ($k = 6.014 \times 10^{-3}$ min^{-1}). The corresponding half-life values indicate a sixteen-fold enhancement in degradation efficiency under optimized conditions (τ = 7 min) relative to the initial state (τ = 115 min). After the 4-hour experimental period, the degradation yield reached 100%, confirming the effectiveness of the optimized process.

To explore the photocatalytic performance of the zinc-aluminum-doped spinel ferrite, the study focused on developing PVDF-based polymer nanocomposites, offering an efficient strategy for catalyst recovery and reuse while overcoming the limitations associated with its use in powder form. Embedding the spinel ferrite within polymer matrices enhances material stability and handling, thereby broadening its applicability in wastewater treatment.

The novelty introduced in this doctoral thesis lies in the development of two PVDF-based nanocomposites designed for pollutant photodegradation under visible-light irradiation. The polymeric materials **10ZnAlFeSm6/PVDF** and **20ZnAlFeSm6/PVDF** were obtained via electrospinning, using poly(vinylidene fluoride) (PVDF) as the polymeric support and $ZnAlFe_{0.94}Sm_{0.06}O_4$ (ZnAlFeSm6) as the inorganic filler.

SEM analysis revealed a porous morphology with randomly oriented fibers, while X-ray diffraction and EDX elemental mapping confirmed the uniform dispersion of the spinel ferrite within the polymer structure. The electrospun membranes exhibited paramagnetic behavior, and mechanical analysis showed that the incorporation of **ZnAlFeSm6** nanoparticles increased polymer-chain rigidity while simultaneously enhancing the specific surface area and pore size—factors that collectively contributed to improved photocatalytic activity.

The electrospun nanocomposites achieved photodegradation efficiencies of 80–98% for methylene blue under visible light over 600 minutes. Experimental results demonstrated that **10ZnAlFeSm6/PVDF** (0.50% w/v) achieved the highest rate constant ($k = 5.413 \times 10^{-3}$ min^{-1}) and maintained stable performance over five consecutive reuse cycles. Reactive species trapping experiments identified the superoxide radical as the dominant active species in the photodegradation mechanism.

Chapter 4

The design of modified manganese ferrites with the general formula $MnFe_{2-x}RExO_4$ (RE = La, Ce, Gd, and Er; x = 0 and 0.04), together with the development of carboxymethyl cellulose-based nanocomposites, introduces a significant element of novelty to this work. This approach highlights the sustainability and biodegradability of CMC, combined with magnetic separability, low cost, accessible synthesis, durability, and complementary adsorption and photocatalytic properties. Consequently, the three-material series were employed for both catalytic and sorptive applications.

The manganese-based spinel ferrites were synthesized via the sol–gel auto-combustion method, enabling the efficient incorporation of rare-earth cations into the spinel lattice. XRD and TEM analyses confirmed the formation of a pure spinel phase. TEM microscopy revealed uniformly distributed nanometric particles with a pronounced tendency toward agglomeration due to their superparamagnetic behavior.

Wet catalytic tests using hydrogen peroxide demonstrated remarkable removal efficiencies, achieving over 97% degradation of Orange II within 30 minutes at 343 K. The pseudo-first-order rate constants were in the 10^{-1} min^{-1} range, with $MnFe_{1.96}Gd_{0.04}O_4$ (**MnFeGd**) exhibiting the highest catalytic activity ($k = 1.364 \times 10^{-1}$ min^{-1}). At lower temperatures of 333 K and 323 K, the PFO rate constants decreased to the 10^{-2} min^{-1} range, indicating reduced degradation efficiency.

Activation-energy analysis revealed lower values for the rare-earth-doped samples (51.17–58.35 kJ/mol) compared to undoped manganese ferrite (70.45 kJ/mol), with Er-doped ferrite exhibiting the lowest activation energy (51.17 kJ/mol), confirming the strong influence of doping on catalytic reactivity. Furthermore, total organic carbon measurements showed that the **MnFeEr** sample ($MnFe_{1.96}Er_{0.04}O_4$) achieved the highest degree of mineralization (70.60%), demonstrating its superior efficiency in pollutant degradation.

Another innovative component of this doctoral thesis is the use of sodium carboxymethyl cellulose (**CMC**) as a natural polymeric support, offering a sustainable alternative for wastewater decontamination. Owing to its biodegradability, chemical compatibility, and functional versatility, CMC enables the development of efficient composites capable of adsorbing and degrading organic pollutants from aqueous solutions.

To optimize stability and porosity, the CMC-based composites were synthesized via ionotropic gelation, using metal cations to reinforce the polymer network. Additionally, ionic crosslinking was employed to enhance mechanical strength and improve adsorption and photocatalytic performance, resulting in superior efficiency in water purification processes. To facilitate magnetic separation of the sorbents, $MnFe_2O_4$ nanoparticles synthesized through sol–gel auto-combustion were incorporated into the hydrogel matrix. The surfactant SDS was further introduced as a porogenic agent, increasing both adsorption capacity and hydrodynamic stability. The SDS-modified magnetic nanocomposites (**CMC/MnFe–S1**, **CMC/MnFe–S2**, **CMC/MnFe–S3**) were subjected to morphological, structural, and magnetic characterization. Among these, **CMC/MnFe–S2** exhibited adsorption kinetics consistent with the PFO model, achieving a maximum adsorption capacity of 234 mg/g at 300 K. Langmuir isotherms confirmed homogeneous adsorption, while thermodynamic parameters indicated a spontaneous ($\Delta G < 0$) and exothermic ($\Delta H < 0$) process. The sorbent was recovered with 93% efficiency and successfully reused.

The ionotropic gelation process enabled the synthesis of a new series of nanocomposites based on carboxymethyl cellulose and modified manganese spinel ferrites (**CMC/MnFe**, **CMC/MnFeLa**, **CMC/MnFeCe**, **CMC/MnFeGd**, **CMC/MnFeEr**), modified for enhanced pollutant photodegradation. The influence of the inorganic fillers is reflected in the altered morphological characteristics, specifically the reduction in granule size (from 2.69 to 1.89 mm) and the formation of surface aggregates. Representative surface micrographs reveal smooth morphologies with a uniform dispersion of the inorganic phase, while cross-sectional SEM images show ferrites homogeneously distributed throughout the

porous cellulose layers. These observations confirm that the incorporated inorganic components significantly increase the porosity of the resulting materials.

Photodegradation experiments using methylene blue under UV–Vis irradiation demonstrated efficiencies ranging from 63% to 99.6% under UV light, with ferrite-containing composites exhibiting superior performance. Experimental calculations further showed that the nanocomposites possess higher rate constants than the photolysis process conducted without a polymeric catalyst, confirming the favorable influence of rare-earth cations on photocatalytic activity.

Among the spherical nanocomposites, **CMC/MnFeCe** displayed the highest rate constant and the shortest half-life ($k = 16.24 \times 10^{-4}$ min^{-1}, $\tau_{1/2} = 0.0427 \times 10^{4}$ min). These findings indicate that nanoscale parameters—such as lattice characteristics, interplanar spacing, and particle size—play decisive roles in determining the photocatalytic efficiency of the synthesized materials.

Reactive species trapping experiments further clarified the mechanism of action. The addition of IPA caused a slight decrease in degradation efficiency, confirming the moderate involvement of hydroxyl radicals (HO•). The most pronounced inhibitory effect was observed upon the introduction of HQ, which significantly reduced photocatalytic activity and indicated that superoxide radicals ($\bullet O_2^-$) are the dominant reactive species generated by the magnetic component dispersed along the carboxycellulose chains.

Based on these results, a reaction mechanism for MB photodegradation was proposed. UV irradiation promotes electron excitation from the valence band to the conduction band, generating electron–hole pairs. These species interact with molecular oxygen and water, forming reactive oxygen species (superoxide and hydroxyl radicals). The radicals subsequently attack MB molecules, producing small intermediates, H_2O, CO_2, SO_4^{2-}, and N_2. A fraction of the photogenerated electrons is captured by the polysaccharide chains, limiting electron–hole recombination and thereby enhancing photocatalytic efficiency.

Selective references

1. Pascariu P, Cojocaru C. Innovative Materials Produced by the Electrospinning-Calcination Method for Advanced Oxidation. IGI Global, p. 250-77, **2023**.
7. Bopape DA, Ntsendwana B, Mabasa FD. Photocatalysis as a pre-discharge treatment to improve the effect of textile dyes on human health: A critical review. Heliyon, *10*(20), e39316, **2024**.
10. Mishra V, Mukherjee P, Bhattacharya S, Sharma RS. Innovative sustainable solutions for detoxifying textile industry effluents using advanced oxidation and biological methods. Journal of Environmental Management, *380*, 124804, **2025**.
11. Zhang Y, Yu H, Zhai R, Zhang J, Gao C, Qi K, Yang L, Ma Q. Recent Progress in Photocatalytic Degradation of Water Pollution by Bismuth Tungstate. Molecules, *28*(24), 8011, **2023**.
124. Samoila P, Cojocaru C, Cretescu I, Stan CD, Nica V, Sacarescu L, Harabagiu V. Nanosized Spinel Ferrites Synthesized by Sol-Gel Autocombustion for Optimized Removal of Azo Dye from Aqueous Solution. Journal of Nanomaterials, *2015*, 1-13, **2015**.
227. Grecu I, Enache A-C, Pascariu P, Bele A, Samoila P, Cojocaru C, Harabagiu V. Modified spinel ferrite–based composite membranes with highly proficient photocatalytic activity. Surfaces and Interfaces, *51*, 104536, **2024**.
247. Grecu I, Samoila P, Pascariu P, Cojocaru C, Dascalu IA, Harabagiu V. Enhanced Photodegradation of Organic Pollutants by Novel Samarium-Doped Zinc Aluminium Spinel Ferrites. Catalysts, *13*, 266, **2023**.
248. Samoilă P, Lupei M, Grecu I, Cojocaru C, Ioniță D, Harabagiu V, inventorsCatalizatori și Metode Pentru Depolimerizarea Deșeurilor De Polietilen Teraftalat Prin Procese De Glicoliză. România2024 30.05.2024.
249. Enache A-C, Grecu I, Samoila P, Cojocaru C, Harabagiu V. Magnetic Ionotropic Hydrogels Based on Carboxymethyl Cellulose for Aqueous Pollution Mitigation. Gels, *9*(5), 358, **2023**.
253. Samoila P, Cojocaru C, Sacarescu L, Dorneanu Pascariu P, Domocos AA, Rotaru A. Remarkable catalytic properties of rare-earth doped nickel ferrites synthesized by sol-gel auto-combustion with maleic acid as fuel for CWPO of dyes. Applied Catalysis B: Environmental, *202*, 21–32, **2017**.
272. Zhang J, Song J-M, Niu H-L, Mao C-J, Zhang S-Y, Shen Y-H. ZnFe2O4 nanoparticles: synthesis, characterization, and enhanced gas sensing property for acetone. Sens Actuators B: Chem, *221*, 55-62, **2015**.
273. Ignat M, Samoila P, Cojocaru C, Sacarescu L, Harabagiu V. Novel Synthesis Route for Chitosan-Coated Zinc Ferrite Nano particles as Potential Sorbents for Wastewater Treatment (Chitosan-ZnFe2O4 Sorbent for Wastewater Treatment). Chem Eng Commun, *203*, 1591-9, **2016**.
275. Slimani Y, Almessiere MA, Guner S, Aktas B, Shirsath SE, Silibin MV, Trukhanov AV, Baykal A. Impact of Sm(3+) and Er(3+) Cations on the Structural, Optical, and Magnetic Traits of Spinel Cobalt Ferrite Nanoparticles: Comparison Investigation. ACS Omega, *7*(7), 6292-301, **2022**.
276. Xavier S, Thankachan S, Jacob BP, Mohammed EM. Effect of Samarium Substitution on the Structural and Magnetic Properties of Nanocrystalline Cobalt Ferrite. Journal of Nanoscience, *2013*, 1-7, **2013**.
285. Adarsha JR, Ravishankar TN, Manjunatha CR, Ramakrishnappa T. Green synthesis of nanostructured calcium ferrite particles and its application to photocatalytic degradation of Evans blue dye. Materials Today: Proceedings, *49*, 777-88, **2022**.

286. Jinendra U, Bilehal D, Nagabhushana BM, Jithendra Kumara KS, Kollur SP. Nano-catalytic behavior of highly efficient and regenerable mussel-inspired Fe(3)O(4)@CFR@GO and Fe(3)O(4)@CFR@TiO(2) magnetic nanospheres in the reduction of Evans blue dye. Heliyon, *7*(1), e06070, **2021**.
296. Pascariu P, Cojocaru C, Samoila P, Olaru N, Bele A, Airinei A. Novel electrospun membranes based on PVDF fibers embedding lanthanide doped ZnO for adsorption and photocatalytic degradation of dye organic pollutants Materials Research Bulletin, *141*, 111376, **2021**.
297. Pascariu P, Cojocaru C, Homocianu M, Samoila P, Grecu I, Bele A. New composite membranes based on PVDF fibers loaded with TiO2: Sm nanostructures and reinforced with graphene/graphene oxide for photocatalytic applications. Surfaces and Interface, *34*, 102382, **2022**.
304. Wang W, Sun H. Effect of different forms of nano-ZnO on the properties of PVDF/ZnO hybrid membranes. Journal of Applied Polymer Science, *137*(36), 49070, **2020**.
307. Cai X, Lei T, Sun D, Lin L. A critical analysis of the α, β and γ phases in poly(vinylidene fluoride) using FTIR. RSC Advances, *7*(25), 15382-9, **2017**.
308. Zhang Y, Xiao Q, Lei G, Li Z. An investigation of a novel MnO2 network-Ni/PVDF double shell/core membrane as an anode for lithium ion batteries. Physical Chemistry Chemical Physics, *17*(28), 18699-704, **2015**.
310. Li J, Meng Q, Li W, Zhang Z. Influence of crystalline properties on the dielectric and energy storage properties of poly(vinylidene fluoride). Journal of Applied Polymer Science, *122*(3), 1659-68, **2011**.
312. Zhao Y, Yang W, Zhou Y, Chen Y, Cao X, Yang Y, Xu J, Jiang Y. Effect of crystalline phase on the dielectric and energy storage properties of poly(vinylidene fluoride). Journal of Materials Science: Materials in Electronics, *27*, 7280-6, **2016**.
315. Pascariu P, Airinei, A, Olaru N, Rosca I., Koudoumas E, Suchea, MP. Innovative Ag–TiO2 nanofibers with excellent photocatalytic and antibacterial actions. Catalysts, *11*, 1234, **2021**.
323. Pollard ZA, Karod M, Schmitz A, Pian B, Barstow B, Goldfarb JL. ZnO Precursor's ability to catalyze formation of reactive oxygen species to degrade aqueous organic pollutants. Chemical Engineering Journal, *480*, 147499, **2024**.
352. Rather S-U, Saeed U, Al-Zahrani AA, Bamufleh HS, Alhumade HA, Taimoor AA, Lemine OM, Ali AM, Al Zaitone B, Alam MM. Doped Nanostructured Manganese Ferrites: Synthesis, Characterization, and Magnetic Properties. Journal of Nanomaterials, 2021, 9410074, 2021.
353. Kamran M, Anis-ur-Rehman M. Enhanced transport properties in Ce doped cobalt ferrites nanoparticles for resistive RAM applications. Journal of Alloys and Compounds, 822, 153583, 2020.
354. Naveena G, Ravinder D, Babu TA, Reddy BR, Sumalatha E, Vani K, Rajender T, Prasad NVK. Low-temperature magnetic properties of erbium doped bismuth nano-ferrites. Journal of Materials Science: Materials in Electronics, 32(13), 18224-30, 2021.
355. Zhou X, Wang J, Yao D. Effect of rare earth doping on magnetic and dielectric properties of NiZnMn ferrites. Journal of Alloys and Compounds, 935, 167777, 2023.
356. Ikram S, Jacob J, Mehboob K, Mahmood K, Amin N, Arshad MI, Ajaz un Nabi M. Role of Rare Earth Metal Ions Doping on Structural, Electrical, Magnetic, and Dielectric Behavior of Spinel Ferrites: a Comparative Study. Journal of Superconductivity and Novel Magnetism, 34(7), 1833-42, 2021.
364. Torquato M, da Silva Neto EG, de Assis Verly Heringer M, Baggio-Saitovich EM, Viana ER, de Biasi RS. Cerium doped superparamagnetic Mn–Zn ferrite particles as a promising

material for self-regulated magnetic hyperthermia. Journal of Materials Research and Technology, *33*, 7380-90, **2024**.
365. Akter S, Khan MNI, Ferdous F, Das HN, Alam MK, Rahman MA, Hasan T, Syed IM. Unveiling the role of sintering temperatures in the physical properties of Cu-Mg ferrite nanoparticles for photocatalytic application. Heliyon, *10*(23), e40771, **2024**.
370. Ma J, Liu C, Chen K. Insight in the relationship between magnetism of stoichiometric spinel ferrites and their catalytic activity. Catalysis Communications, *140*, 105986, **2020**.

Publications and Scientific Contributions

Articles published in International Specialty Journals relevant to the doctoral thesis:

1. **Grecu I**, Cojocaru C, Ignat M, Dascalu AI, Silion, M, Enache A-C, Harabagiu V, Samoilă P. Understanding Catalytic Wet Peroxide Oxidation of organic pollutants by exploring new Rare-Earth Doped Manganese Spinel Ferrites. Journal of Environmental Chemical Engineering, *13*,119496, **2025.** https://doi.org/10.1016/j.jece.2025.119496 (f_i = 7,4, Q1);
2. **Grecu I**, Enache, A-C, Pascariu P, Bele A, Samoilă P, Cojocaru C, Harabagiu V. Modified spinel ferrite–based composite membranes with highly proficient photocatalytic activity. Surfaces and Interfaces, *51*, 104536. **2024**. https://doi.org/10.1016/j.surfin.2024.104536. (f_i = 5,7, Q1);
3. Enache A-C, **Grecu I**, Samoilă P, Cojocaru C, Harabagiu V. Magnetic Ionotropic Hydrogels Based on Carboxymethyl Cellulose for Aqueous Pollution Mitigation. Gels, *9*(5), 358, **2023**. https://doi.org/10.3390/gels9050358. (f_i = 5,0, Q1).
4. **Grecu I**, Samoilă P, Pascariu P, Cojocaru C, Dascălu I-A, Harabagiu V. Enhanced Photodegradation of Organic Pollutants by Novel Samarium-Doped Zinc Aluminium Spinel Ferrites. Catalysts, *13*, 266, **2023**. https://doi.org/10.3390/catal13020266. (f_i = 3,8, Q2);

Invention Patent Applications Associated with the Doctoral Research Topic:

1. Samoilă P, Lupei M, **Grecu I**, Cojocaru C, Ioniță D, Harabagiu V. Catalizatori și Metode Pentru Depolimerizarea Deșeurilor De Polietilen Teraftalat Prin Procese De Glicoliză. **RO-BOPI 5/2024** din 30.05.2024.

Papers Published in ISI-Indexed Journals (Results not included in the thesis):

1. Enache A-C, **Grecu I,** Samoilă P. Polyethylene Terephthalate (PET) Recycled by Catalytic Glycolysis: A Bridge toward Circular Economy Principles. Materials, *17*, 2991, **2024**. https://doi.org/10.3390/ma17122991. (f_i = 3,1, Q3).
2. Pascariu P, Cojocaru C, Homocianu M, Samoilă P, **Grecu I**, Bele A. New composite membranes based on PVDF fibers loaded with TiO_2: Sm nanostructures and reinforced with graphene/graphene oxide for photocatalytic applications. Surfaces and Interfaces, *34*, 102382, **2022**. https://doi.org/10.1016/j.surfin.2022.102382. (f_i = 5,7, Q1);
3. Samoilă P, **Grecu I**, Asandulesa M, Cojocaru C, Harabagiu V. Bio-based ionically cross-linked alginate composites for PEMFC potential applications. Reactive and Functional Polymers. *165*, 104967, **2021**. https://doi.org/10.1016/j.reactfunctpolym.2021.104967. (f_i = 4,5, Q1);

Oral presentations at national and international scientific events:

1. **Ionela Grecu**, Petrișor Samoilă, Corneliu Cojocaru, Petronela Pascariu, Valeria Harabagiu, "*Manganese ferrite-based materials for catalytic applications*", a 4-a ediție a conferinței "ICMPP - Open Door to The Future Scientific Communications of Young Researchers", MacroYouth'2023, Iași, România, 17 noiembrie 2023;
2. Andra-Cristina Enache, **Ionela Grecu**, Petrișor Samoilă, Corneliu Cojocaru, Valeria Harabagiu, "*Magnetic ionotropic hydrogels for water pollution mitigation*", a 29-a ediție a Conferința Internațională "Progress in Organic and Macromolecular Compounds", Iași, România, 4 – 6 octombrie 2023;

3. **Ionela Grecu**, Petrișor Samoilă, Corneliu Cojocaru, Petronela Pascariu, Maria Ignat, Daniela Ioniță, Mihai Lupei, Valeria Harabagiu, "*Catalytic behaviour of doped manganese ferrite with spinel structure*", a 25-a ediție a Conferinței internaționale "Materials, Methods & Technologies", International Scientific Events 2023, Burgas, Bulgaria, 17– 20 august 2023;
4. **Ionela Grecu**, Petrișor Samoilă, Corneliu Cojocariu, Petronela Pascariu, Valeria Harabagiu, "*Synthesis and characterization of new doped manganese ferrites by sol-gel auto-combustion method*", a 3-a ediție a conferinței "ICMPP - Open Door to The Future Scientific Communications of Young Researchers", MacroYouth'2022, 3rd edition, Iași, România, 18 noiembrie 2022;
5. **Ionela Grecu**, Petrișor Samoilă, Corneliu Cojocariu, Petronela Pascariu, Valeria Harabagiu, "Enhanced photodegradation of Evans Blue by novel samarium doped zinc aluminium spinel ferrites", a 2-a ediție a conferinței "ICMPP - Open Door to The Future Scientific Communications of Young Researchers", MacroYouth'2021, Iași, România, 19 noiembrie 2021;
6. Valeria Harabagiu, Petrișor Samoilă, Răzvan Rotaru, **Ionela Grecu**, "*Polysaccharide composites – energy related applications*", a 23-a ediție a Conferinței internaționale "New Cryogenic and Isotope Technologies for Energy and Environment" - EnergEn 2021, Băile Govora, Vâlcea, România, 26 – 29 octombrie 2021;
7. **Ionela Grecu**, Petrișor Samoilă, Corneliu Cojocariu, Petronela Pascariu, Valeria Harabagiu, *"Novel zinc aluminium spinel ferrites. Synthesis and photocatalytic properties for Evans Blue degradation"*, a 3-a ediție a "International Workshop Advances on Photocatalysis including Environmental and Energy Applications", AdvPhotoCat-EE 2021, Creta, Grecia, 28 – 29 iunie 2021;
8. **Ionela Grecu**, Petrișor Samoilă, Corneliu Cojocaru, Valeria Harabagiu, *"Alginate-based membranes with possible applications in fuel cells"*, prima ediție a conferinței "ICMPP - Open Door to The Future Scientific Communications of Young Researchers", MacroYouth'2020, Iaşi, România, 19 noiembrie 2020.

Poster presentations at national and international scientific events:

1. **Ionela Grecu**, Petrisor Samoila, Corneliu Cojocaru, Andra-Cristina Enache, "Development Of Novel Spinel-Type Mixed Oxides To Achieve Circularity In Bio-Based Sorbents", a 25-a ediție a Simpozionului Internațional "Industria și Mediul", București, România, 23-24 octombrie 2025;
2. **Ionela Grecu1**, Andra-Cristina Enache, Petrisor Samoila, Corneliu Cojocaru, Bogdan-Constantin Condurache, Petronela Pascariu, Valeria Harabagiu, *"Engineering Spinel-Type Mixed Oxides for Potential Wastewater Applications"*, a 27-a ediție a Conferinței internaționale "Materials, Methods & Technologies", International Scientific Events 2025, Burgas, Bulgaria, 14– 17 august 2025;
3. **Ionela Grecu**, Andra-Cristina Enache, Petronela Pascariu, Petrișor Samoilă, Corneliu Cojocaru, Adrian Bele, Valeria Harabagiu, *"Ferrite/PVDF composite membranes with high photocatalytic properties"*, a 5-a ediție a conferinței internaționale "ICMPP - Open Door to The Future Scientific Communications of Young Researchers", MacroYouth'2024, Iaşi, România, 15 noiembrie 2024;
4. **Ionela Grecu**, Petrișor Samoilă, Corneliu Cojocaru, Petronela Pascariu, Maria Ignat, Daniela Ioniță, Mihai Lupei, Valeria Harabagiu, "*Development of mixed oxides with spinel structure via the sol-gel auto-combustion technique*", a 25-a ediție a

Conferinței internaționale "Materials, Methods & Technologies", International Scientific Events 2023, Burgas, Bulgaria, 17– 20 august 2023;

5. Petronela Pascariu, **Ionela Grecu**, Enache Andra-Cristina, Petrișor Samoilă, Corneliu Cojocaru, Maria Ignat, Mihai Lupei, Valeria Harabagiu, "*Modified nanosized spinel ferrite-based materials with highly proficient catalytic activitiy*", a 4-a ediție a "International Workshop Advances on Photocatalysis including Environmental and Energy Applications", AdvPhotoCat-EE2023, Heraklion, Creta, Grecia, 25-28 iulie 2023;
6. **Ionela Grecu**, Petrișor Samoilă, Corneliu Cojocaru, Petronela Pascariu, Valeria Harabagiu, "Synthesis and characterization of new doped manganese ferrites by sol-gel auto-combustion method", a 36-a ediție a Conferinței Naționale de Chimie 2022, CNCHIM – 2022, Călimănești – Căciulata, România, 5 – 7 octombrie 2022;

Team member in the national research projects:

1. "Bio-nanocomposite formulations – kaempferol encapsulated in eutectic solvents for corneal regeneration," acronym: BIODESKMP, project code: PN-IV-PCB-RO-MD-2024-0372, funding contract: 13PCBROMD/2025;
2. "Polymeric and hybrid systems for exploring and enhancing the removal of organic pollutants from contaminated waters," acronym: POLHSYS, project code: PN-IV-P1-PCE-2023-0144, funding contract: 86PCE/2025;
3. "Hybrid/composite biomaterials with magnetic susceptibility for the depollution of contaminated waters," acronym: BIOHYCLEAN, project code: PN-IV-P2-2.1-TE-2023-1830, funding contract: 73TE/1.03.2025;
4. "Advances in the Chemical Recycling of PET Waste – Catalytic Glycolysis Using Nanoscale Magnetic Catalysts," acronym: PET-Rec, project code: PN-III-P1-1.1-TE-2021-0030, funding contract: TE 21/2022;
5. "New nanostructured composite membranes with enhanced photocatalytic properties for water purification," acronym: CleanH2O, project code: PN-III-P1-1.1-TE-2019-0594, funding contract: TE164/2020;
6. "The engine of the hydrogen-based energy revolution – Fuel cells on the pathway from research to production through the minimization of technological barriers," acronym: ROFCC, project code: PN-III-P1-1.2-PCCDI-2017-0194, funding contract: 25PCCDI/21.03.2018.